AN ABSTRACT OF THE THESIS OF

Fatih Sen for the degree of Master of Science in Civil Engineering presented on February 2, 2023.

Title: Assessing the Feasibility of Utilizing UAS-Based Point Clouds for Pavement Smoothness/Roughness Quantification

Abstract approved: ____

Erzhuo Che, Michael J. Olsen

Transportation agencies continuously strive to improve driving quality and highway safety, which are both highly correlated with the level of smoothness of the road. The International Roughness Index (IRI) is a widely adopted, standardized metric calculated from longitudinal profile data collected on the road. Inertial profilers are devices mounted to vehicles that are commonly utilized by transportation agencies to determine the IRI. However, inertial profilers have a narrow field of view and relatively low positioning accuracy, resulting in a lack of context of the conditions across the road surface. In contrast, remote sensing techniques such as Structure of Motion (SfM) Multi-view Stereopsis MVS) photogrammetry or lidar from an uncrewed aircraft system (UAS) have the ability to efficiently and safely capture detailed 3D texture information across the road surface. Nevertheless, there is still a need to examine the accuracy of determining the pavement roughness (e.g., IRI) with UAS SfM/MVS data. To this end, this study (1) assesses the accuracy of UAS SfM/MVS photogrammetric data, (2) establishes a framework to extract IRI metrics from point cloud data, and (3) explores factors that can impact the quality of point cloud data, such as the flight plan, weather conditions, sensor calibrations, and so forth through a detailed case study.

Keywords: International Roughness Index (IRI); UAS-SfM/MVS; Pavement Roughness; Vertical accuracy assessment; Terrestrial lidar, Drones

Assessing the Feasibility of Utilizing UAS-Based Point Clouds for Pavement Smoothness/Roughness Quantification

by
Fatih Sen

A THESIS

submitted to

Oregon State University

in partial fulfillment of
the requirements for the
degree of

Master of Science

Presented February 2, 2023
Commencement June 2023

Master of Science thesis of Fatih Sen presented on February 2, 2023

APPROVED:

Co-Major Professor, representing Civil Engineering

Co-Major Professor, representing Civil Engineering

Head of the School of Civil and Construction Engineering

Dean of the Graduate School

I understand that my thesis will become part of the permanent collection of Oregon State University libraries. My signature below authorizes release of my thesis to any reader upon request.

Fatih Sen, Author

ACKNOWLEDGEMENTS

Throughout the course of completing this study, I have received a substantial amount of support and guidance, and I would want to acknowledge and convey my gratitude to those individuals.

First and foremost, I want to convey my thanks and admiration to my graduate advisors, Professor Dr. Michael Olsen and Dr. Erzhuo Che, for their unending guidance, support, and patience during this entire process. Thank you, Professor Olsen, for your support throughout my time at OSU and for allowing me to become a member of the OSU geomatics family. Dr. Che, you were an invaluable resource for me during my master's program at Oregon State University, providing informative comments at each level of my study and encouraging me to move forward.

I would also like to express my appreciation to Prof. Mike Bailey and Chase Simpson for taking the time to be on my committee.

I would also want to thank Chase Simpson and Andrew Senogles for their support and, in particular, their cooperation with data acquisition and the contribution of their expertise to data processing.

I must express my deep gratitude to the Ministry of National Education of the Republic of Turkey for sponsoring my graduate education; without the scholarship, this would not have been possible.

Thank you to ODOT and PacTrans for providing funds and permission for data acquisition.

Thanks to Cloud Compare, Leica Geosystems, and David Evans & Associates for providing the surveying equipment and processing software.

Finally, I would like to express my sincere thanks to my family and my fellow geomatics students for their constant support and belief in me.

TABLE OF CONTENTS

Page

TABLE OF CONTENTS (Continued)

LIST OF FIGURES

LIST OF TABLES

LIST OF APPENDICES

CHAPTER 1. INTRODUCTION

1.1 Background

In order to ensure travelers' comfort, safety, and fuel efficiency, roadways must not only be functional but must be in decent condition (Louhghalam et al., 2015). To achieve performance goals, the Pavement Management System (PMS) is an automated system that transportation agencies heavily rely on to monitor and assess road surface conditions, which aids decision-makers in making consistent, cost-effective decisions through good management practices to maintain pavements in serviceable condition (Ragnoli et al., 2018). Roughness statistics, along with surface distress, skid resistance, rutting, and structural capacity, are among the most critical aspects for pavement management systems when analyzing pavement data. Surface roughness, in general, refers to the degree to which a road's surface deviates from a perfectly flat plane along axes such as a longitudinal profile, transverse profile, or cross slope. Deteriorated pavement surfaces tend to have higher surface roughness (Fakhri et al., 2021); as a result, smooth pavements have numerous advantages, such as: requiring less maintenance; being safer; resulting in less dynamic stress on vehicles compared with roads with a rough surface, which provides environmental benefits such as higher fuel efficiency and less wear on vehicles; lasting longer; and being more solid (De Blasiis et al., 2020a; ASTM E1926-08, 2021).

1.1.1 Road roughness indices

Numerous roughness dynamic indices have been used to determine the roughness/ smoothness of a pavement surface. The most common ones are the International Roughness Index (IRI), the Profilograph Index (PrI), the Quarter-car Index, the root-mean-square vertical acceleration, and the rod and level surface smoothness measurement (Zak, 2016). Among these indices, IRI was established in 1982 through a joint effort involving institutions from around the globe, road maintenance departments and agencies, research institutes, and the World Bank in order to standardize the measurement of roughness across organizations and eliminate the inconsistencies that had previously resulted from the use of different instruments and approaches (Sayers, 1986). It has become the most extensively used roughness index (Olsen & Chin, 2012a; Múčka, 2017; Cruz et al., 2021; Karamihas, 2021) due to its reproducibility and stability over time (Sayers, 1998). Currently, the majority of US State Departments of Transportation (DOTs) use IRI to evaluate pavement roughness (Ong et al., 2010; Smith & Ram, 2016). The World Bank has taken ownership of the definition of standards and recommendations for this index (Thomas, 2021).

The ASTM E1926-08 standard defines IRI as mathematical processing of longitudinal profile data to provide road roughness statistics, which correspond to cumulative units of slope suspension motions divided by the distance traveled with a quarter-car model at 80 km/h (50 mph) speed (Cruz et al., 2021; ASTM E1926-08, 2021). This quarter-car model (also known as the Golden Car) models the impact of a single tire system on the road surface. It comprises one wheel represented by a vertical spring, axle mass supported by the tire, a suspension spring and damper, and vehicle body mass supported by the suspension (Sayers, 1989). As a result, it is typically stated as a ratio, such as meters per kilometer or inches per mile (**Figure 1.1**)

Some important considerations for determining the IRI value are listed as follows based on previous studies:

- The IRI calculation relies on the longitudinal profile qualities being measured accurately; hence, the elevation profile measuring equipment utilized in this technique must have sufficient accuracy and resolution, particularly at the local, relative measurement level (Olsen & Chin, 2012a; Chin & Olsen, 2014).
- The precision of the IRI depends on the interval (i.e., distance) between consecutive profile elevation measurements; hence, decreasing the spacing often improves precision. A maximum interval of 0.3 m (12 in.) is recommended by ASTM standards (ASTM E1926-08, 2021)
- A moving average filter uses a low pass filter of 9.85 in (250 mm) to smooth the profile by using the average values of adjacent points to simulate the tire encircling effect of tires (Sayers, 1998).
- Particularly rough areas can be lost in the averaging process when computing IRI over a large distance. Hence, localized roughness has been defined as any 25-foot (7.62-meter) segment with IRI values that has a disproportionate effect on the overall IRI (AASTHO-R54-10,2010; Olsen & Chin, 2012a).

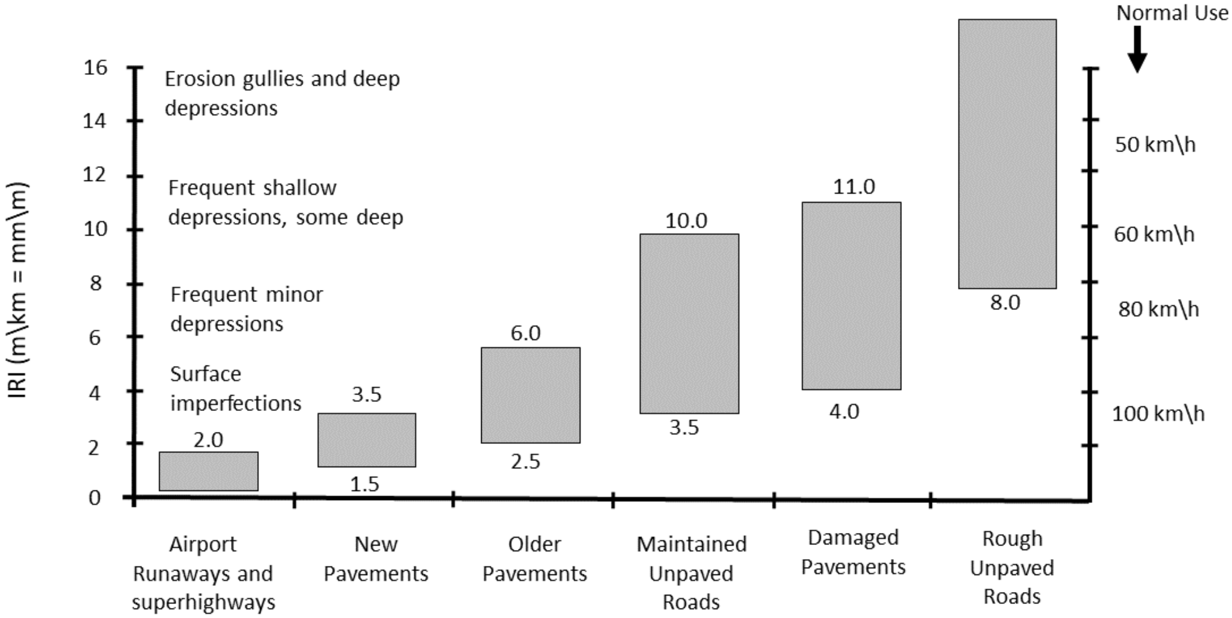

Figure 1.1. The IRI Roughness Scale (Elghriany et al., 2016; Sayers, 1986)

1.1.2 Road profile measurement

Road surface profiles, which capture elevation variations of a road over a certain distance, can be measured using a variety of devices for both new and existing pavements (Olsen & Chin, 2012a). The ASTM E 950-94 standard groups roughness measuring equipment into four classes based on the survey accuracy (Bennett et al.,2006; Radović et al., 2016; Prosser-Contreras et al., 2020; Thomas, 2021);

- **Class 1 -** indicates the highest accuracy and, regardless of speed, corresponds to a longitudinal profile with a vertical precision of 0.5 mm (non-contact lightweight profiling devices, portable laser profilers, dipsticks).
- **Class 2 -** considers alternative profiling strategies for IRI measurement in which a longitudinal profile is required (Profilographs, optical and inertial profilers)
- **Class 3 -** incorporates measurements of correlation, which imply a mathematical calculation is needed to acquire the result, and so represents a lower quality level (e.g., Roadmaster, ROMDAS)
- **Class 4 -** reflects the use of subjective procedures and measurements that have not been calibrated (visual inspection, ride over the section, etc.)

The Rod and Level, inclinometer-based profilers (Walking Profilers etc.), and Profilographs are the conventional tools used for data collecting during roughness evaluations. Each of these conventional methods has some distinct advantages. Rod and level grade surveys combined with static profilometer surveys may produce an exceptionally precise (sub-millimeter) profile of the roadway, which is why it is frequently referred to as the "TRUE profile" (Sayers, 1995; Olsen & Chin, 2012a). However, a key limitation of a rod and level is the time required to capture the data and the relatively poor sampling interval compared with other techniques. Manually controlled walking profilers, or inclinometer-based profilers, are substantially faster than the rod and level technique while often providing a real-time display of the data. Profilographs can collect continuous profile data through a wheel-track (Smith & Ram, 2016).

These conventional methods can suffer from several drawbacks (Olsen & Chin, 2012a). First of all, all the aforementioned measuring instruments and techniques require lane closure or some traffic control. Additionally, only one wheel route can be measured at a time while some systems are limited to their operation speed limit. As a result, it is especially challenging to utilize these systems and techniques for high-traffic routes or a large area as it can be time-consuming and prone to safety hazards. Moreover, sufficient expertise and extensive training are required for the implementation teams to be able to acquire high-quality data efficiently.

Inertial (or Laser) profilers are now one of the widely used instruments for collecting asphalt pavement data among transportation agencies (Ong et al., 2010; Smith & Ram, 2016). These systems utilize an accelerometer to track the frame's (vehicle) motion and noncontact laser sensors to track the frame's relative vertical movement to the road surface at a constant sampling interval. Simultaneously, a distance measuring instrument (DMI) keeps track of the travel distance along the highway during the data collection. The combination of these characteristics produces a longitudinal profile of the road.

Although the inertial and laser profilers provide great accuracy, efficiency, and mobility, they still suffer from a few significant constraints. First and foremost, during the data collection, the speed needs to be consistent and should be faster than 15 km/hr (Sayers, 1998), resulting in challenges in collecting data in locales with substantial traffic (Lee & Chou, 2010) such as urban areas (Loizos & Plati, 2008; Prosser-Contreras et al., 2020). Some studies cope with this by modifying the quarter car model's parameters or filtering the data based on certain criteria (De Blasiis et al., 2020a). However, such methods may increase the workload, require more time for both data collection and processing, and potentially introduce biases or errors in the calculations. Another shortcoming is the variation in the vehicle’s trajectory, which may not precisely align with the road alignment. Although this may not be substantial when computing IRI, these variations in the wheel path across the surface render challenges when attempting to obtain a detailed comparison between elevation profiles to track changes in the road surface (Lee & Chou, 2010). Another drawback of profilers is their intrinsically limited field-of-vision (FOV), resulting in difficulty in obtaining a comprehensive understanding of the overall context of the scene (Olsen & Chin, 2012a; Chin & Olsen, 2014), particularly on roadways that have been significantly damaged. Furthermore, some profilometers struggle in measuring severely damaged or stone/dirt roads due to high-frequency variations (De Blasiis et al., 2020b). Lastly, inertial profilers are relatively more expensive to mobilize compared with emerging technologies such as ground or UAS-based photogrammetric or lidar technologies for evaluating shorter sections.

1.2 Remote sensing technologies

The advent of state-of-the-art remote sensing technology has opened up a substantial window of opportunities for transportation agencies to address some of the aforementioned shortcomings of profilers (De Blasiis et al., 2020b). In contrast to earlier profiling technologies, remote sensing technology can be a much more economical solution as it has been widely used for applications such as topographic mapping, and the data can be re-used for multiple purposes beyond measuring elevations along a profile (Olsen & Chin, 2012a; Olsen, 2013).

1.2.1 Lidar technology

Light detection and ranging (Lidar) are one of the most promising approaches among the remote sensing technologies for use in the built environment at the present time (Schnebele et al., 2015; Barbarella et al., 2019; De Blasiis et al., 2020b) due to its high efficiency and accuracy (Olsen et al., 2009; White et al., 2010). Based on the mounting platform, lidar systems can be usually categorized into airborne laser scanning (ALS), mobile laser scanning (MLS), and terrestrial laser scanning (TLS).

ALS can capture a very large area efficiently and is widely used for topographic mapping (Vosselman & Maas, 2010; Shan & Toth, 2018). However, the point density and measurement accuracy are usually not sufficient for capturing geometric details on the road surface due to the long distance between the system and the objects. It is also not feasible to provide frequent monitoring given its cost and logistics.

MLS and TLS are more suitable tools to capture the road surface and assess the road characteristics, and they also have the benefit of allowing for the acquisition of cross-sections from any portion of the road. Moreover, more and more automated approaches have been developed for a variety of feature extraction tasks to help improve the workability of the laser scanning data (Che et al., 2019). While MLS is more efficient in terms of the data collection speed due to the moving platform (De Blasiis et al., 2020b), TLS provides more flexibility to the operators on the scanning locations, settings, and other factors. There are more studies utilizing TLS for road surveying also because of its accuracy and lower cost when covering a relatively small area (Chin & Olsen 2014; Barbarella et al., 2019). Nonetheless, as Olsen & Chin (2012a) and Chin & Olsen (2014) pointed out in a study comparing different survey methods in quantifying the surface roughness, the data quality of TLS systems can suffer from long-range, oblique angles, intensity saturation, as well as low-reflectance surface.

1.2.2 UAS technology

In recent years, uncrewed aircraft systems (UAS) have become a potential alternative to the aforementioned technologies in many civil infrastructure applications (Dobson et al., 2013), including road pavement condition assessment evaluations (Nappo et al., 2021). UAS technology is rapidly evolving on both the hardware and software fronts and can significantly reduce costs while boosting safety, efficiency, resolution, and accuracy.

Compared to ALS, UAS is able to survey at a much lower altitude to be able to capture improved detail on the road surface with a birds-eye perspective of the region of interest (Fonstad et al., 2013). On the other hand, compared with other ground-based lidar systems, UAS pilots need to stay away from the road and traffic for a safer operation to minimize driver distractions (Barlow et al., 2019). Moreover, the flexibility of the UAS can generally be advantageous to provide access at locations that would otherwise be unsafe for MLS and TLS; however, sometimes the UAS access is limited due to public restrictions. Considering the flight duration and other restrictions according to the Federal Aviation Administration (FAA) laws (e.g., visual contact requirement with the UAS during flight), UAS is ideal for efficiently gathering data for areas less than 2 km^2 (Simpson, 2018).

1.2.3 Structure from Motion/Multiview Stereopsis

Revolutionary photogrammetry techniques including Structure-from-Motion (SfM) and multi-view stereopsis (MVS) have been widely applied as a result of the rapid development of computer vision algorithms. These technologies make it possible to construct 3D models from 2D images by utilizing image processing that applies a collection of algorithms to locate and identify points captured by UAS in a series of photos (Prosser-Contreras et al., 2020) through some software packages (e.g. Agisoft Metashape, Pix4D mapper, Visual SfM)(Voumard et al.,2018; Greenwood et al.,2019) without having the knowledge of the camera's location and orientation or reference points in the scene. It also enables users to automatically resolve or refine calibration issues during the process (Iglhaut et al., 2019). All of these advancements significantly reduce the number of ground control points (GCP) necessary for a successful 3D reconstruction. In principle, real-time kinematic (RTK) or post-processing kinematic (PPK) GNSS measurements obtained on the UAS simultaneously with the flight, sometimes with the aid of an inertial measurement unit (IMU), collected during the flight that records the position and orientation of each camera frame, a general-purpose 3D model can be generated without any GCPs, which can be very beneficial for areas that are difficult to access otherwise. That being said, to ensure the quality of the 3D models, an evenly distributed array of accurately surveyed GCPs across the area of interest is highly recommended (Fonstad et al., 2013). Data products derived from this process can include various types and formats including 3D point cloud, DEMs, orthomosaic images, triangular mesh, and so on.

1.2.4 Pavement Assessment with UAS

As one of today's cutting-edge technologies, UAS has been proven to be a useful tool for conducting accurate surveys (Varbla et al., 2021) and rapidly gained popularity in civil engineering applications. One of the applications is to evaluate pavement distress via measures such as IRI leveraging UAS-SfM/MVS produced point clouds. This section provides an overview of several studies that used 3D point clouds and related techniques for pavement assessment.

To utilize UAS-SfM/MVS as an alternative since it can produce high-quality 3D point clouds, Inzerillo et al. (2018) demonstrated the validity of UAS image-derived 3D models for road condition surveys and analyzing pavement distress deformations. Tan & Li (2019) and Saad & Tahar (2019) utilized oblique images acquired by UAS flying over the asphalt paved road at about 20 meters to detect and measure potholes resulting in centimeter accuracy. More recently, Nappo et al. (2021) used the 3D models reconstructed via UAS-SfM/MVS to evaluate the cracks on asphalt-paved roads exposed to landslides in Como, Italy. The research was able to quantitatively detect and describe longitudinal and transverse cracks wider than 1 cm, and the International Roughness Index (IRI) was computed to classify their severity. Nonetheless, several considerations need to be taken into account when performing pavement evaluation using UAS-SfM/MVS including accuracy, ground control points, flight altitude, surface characteristics, and so on (Javadnejad et al., 2021).

1.2.5 Factors affecting UAS data quality factors

Accuracy of the data products (e.g., point clouds, DEMs, etc.) plays an important role in the 3D representation of the pavement, especially for IRI calculations. A wide variety of factors can affect the accuracy of the data products as revealed in many studies investigating the use of UAS-SfM/MVS point clouds in mapping and surveying applications. Some of the critical factors include the accuracy, number, and distribution of ground control points (GCP), resolution, number, blurriness, noise, overlap percentage of images, complexities, shadow effect, and lighting condition of the texture. Some other considerations such as moving objects in the scene, the presence of dense vegetation, the geometry of camera distribution, and image matching performance can also impact the data quality (Fonstad et al., 2013; Agüera-Vega et al., 2017; Bolkas, 2019; Javadnejad et al., 2021).

One way to ensure the accuracy of the 3D reconstruction result is to set up ground control points (GCP). Liao & Wood (2020) explored how the number and distribution of GCPs can affect IRI values. Although the authors pointed out that the consumer-grade GNSS equipped on the UAS platform does not necessarily improve the data quality, it is worth pointing out that many modern systems support RTK or PPK GNSS providing high precision positioning which can reduce the number of GCPs required to achieve the same accuracy (Prosser-Contreras et al., 2020). Similarly, Agüera-Vega et al., (2017) also presented their study on the impact of the number of Ground Control Points in georeferencing on the accuracy of DEMs and orthomosaic images. This research reveals that increasing the number of GCPs improves horizontal and vertical accuracy. The experiment shows that more GCPs would reduce the uncertainty of the 3D reconstruction process. In addition to the GCPs, Varbla et al. (2021) included flight altitude in their analysis of UAS-SfM/MVS data in detecting road structure deformation. The study concluded that the ideal number of GCPs required decreases as survey altitude increases, which means the georeferencing accuracy starts declining when the recommended number of GCPs is surpassed.

Although in principle, a lower flight altitude can result in higher accuracy and resolution of the 3D point cloud (Saad & Tahar, 2019; Tan & Li, 2019; Romero-Chambi et al., 2020), a UAS flight that is too low can disrupt or distract the traffic causing safety hazards (Hurwitz et al., 2018). As a result, even though some studies demonstrated a very low altitude (e.g., 10 m) can yield very high-resolution 3D point clouds with high accuracy (Prosser-Contreras et al., 2020), such flight parameters would not be applicable to highways that have more damaged pavement and high-volume traffic. In this regard, Zeybek & Biçici (2021) examined the impact of flying height on the accuracy of resulting 3D point clouds for IRI evaluations. The study tested flying heights of 35 and 50 m and found no significant difference in point cloud resolution and IRI evaluation results with low and close flying heights.

Given that the SfM technique relies on the contrast and features of the pavement surface captured in the images, the type of pavement is also a significant factor. Alhasan et al. (2015) compared the accuracy of point clouds acquired with TLS and terrestrial-based SfM for assessing road roughness over different types of surfaces including gravel roads, Portland cement concrete (PCC), and one newly paved asphalt surface. Due to the low contrast and poor reflectivity on the fresh asphalt, there are insufficient points captured for IRI computations in both SfM and TLS data. Ward & Newman (2019) also did a study using UAS-SfM/MVS and lidar to analyze airport pavement roughness based on Boeing Bump Index (BBI) and IRI values. On four distinct surface types—sand-asphalt, dirt, main runway asphalt, and concrete pad—they compared results derived from UAS-SfM/MVS against the lidar data for accuracy assessment. For the sand-asphalt surface and the concrete pad surface, the correlation between lidar and UAS-SfM/MVS approaches utilizing both BBI and IRI parameters was found to be poor; however, the correlation was high for the brownish-colored dirt-strip surface. For the runway asphalt surface, the correlation between lidar and UAS-SfM/MVS data was low when using the BBI parameter but acceptable for the IRI parameter. Furthermore, it should be noted that the illumination conditions on an airfield are more ideal than those on a typical roadway since there are limited vertical obstructions near the airport to cause shadows.

Moreover, even under the same concept, the algorithms and implementations in the SfM/MVS software can be different while the parameter settings have a significant impact on the accuracy of the resulting point clouds (Slocum & Parrish, 2017). Agisoft Metashape and Pix4D Mapper are two of the most well-known commercial SfM-based programs. Zeybek & Biçici (2021) compared them, and concluded that Agisoft Metashape is slightly better in terms of its accuracy and efficiency, but only in their specific testing settings. However, it is challenging to establish a well-controlled experimental setting, especially considering the variant outdoor environment. Fortunately, Slocum & Parrish, (2017) proposed a workflow, named simUAS, that generates virtual UAS surveys in a simulated graphical environment which can be used to test a wide variety of factors (e.g., lighting, texture, topography, flight altitude, camera resolution, etc.). Furthermore, Javadnejad et al. (2021) thoroughly tested several critical factors for dense point clouds in different scenarios. The key point feature distribution was examined as a result of the bundle adjustment process, camera stand-off distances, angle of incidence, brightness, and darkness index for image-based reconstruction. The study found all the aforementioned factors can affect the quality of 3D reconstruction to different degrees.

1.3 Objectives of Study

As discussed in the previous sections, UAS-SfM/MVS can be a great tool for assessing and monitoring a relatively small area, especially for those that are subject to ground movement from geohazards (e.g., landslides, sinkholes, soil collapse) and need frequent maintenance and repair. Such areas usually feature multiple patches of pavement resulting in substantial variation in surface roughness, which in turn generates a variety of errors and artifacts **(Figure 1.2**). Most existing work focuses on road sections with the uniform pavement. Hence, the objectives of this research are to:

(1) Develop a framework for obtaining pavement roughness metrics (e.g., IRI) from UAS-SfM/MVS,

(2) Validate the feasibility of using UAS-SfM/MVS point clouds to assess pavement condition through a rigorous accuracy analysis to evaluate the accuracy of the UAS-SfM/MVS point clouds, DEMs, and derived IRI values by comparison to the TLS scans and control survey results.

(3) Provide recommendations and considerations when utilizing UAS-SfM/MVS for road roughness assessment, including both field practice and procedures in the workflow.

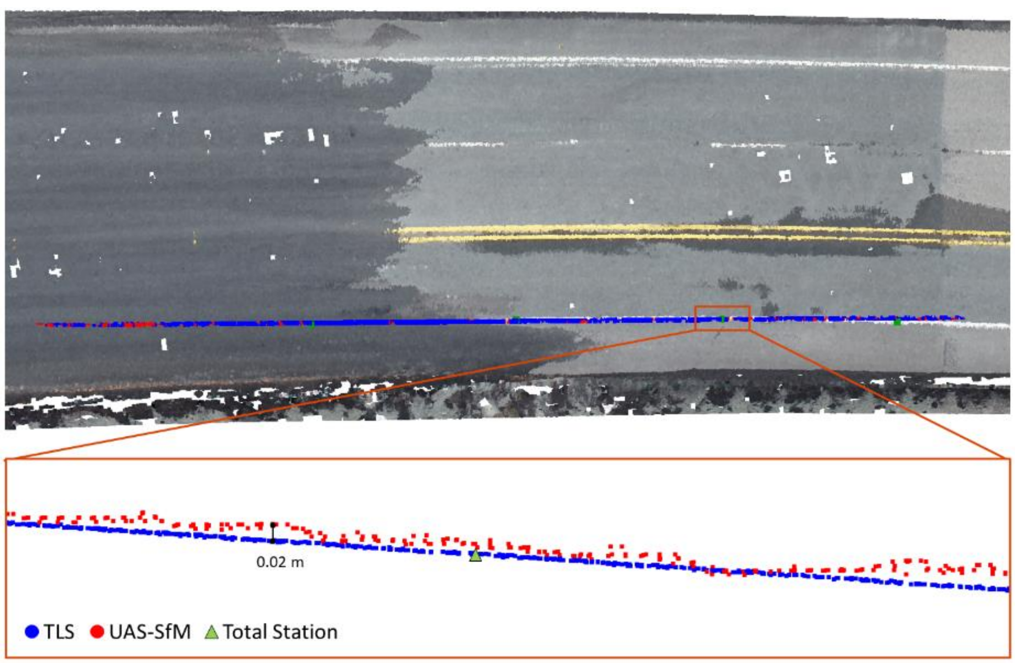

Figure 1.2. Example road profile of TLS and UAS-SfM/MVS point clouds.

CHAPTER 2. MATERIAL & METHODS

2.1 Overview

Field data for this research was collected at the Arizona Inn Landslide site along the Oregon Coast Highway (U.S. Route 101, MP 312) (**Figure 2.1**) on June 14th, 2021. This active slide routinely causes damage to the road surface resulting in frequent repairs and maintenance throughout the year (Olsen et al., 2022; Senogles et al., 2022). The research team acquired aerial photos with UAS and generated point clouds utilizing SfM/MVS photogrammetric processing techniques. The point clouds were then converted into a digital terrain model (DEMs), which was then used to calculate the roughness/smoothness metrics (i.e., IRI) of the road surface. In addition, total station (TS) measurements on the road surface and terrestrial lidar scans (TLS) were collected for comparison and analysis. The equipment used in the field effort is provided in **Table 2.1.**

Table 2.1. Key equipment list for the field effort

INSTRUMENT LIST
Riegl VZ400 Laser Scanner with Nikon D700 Digital Camera
Leica GS14 GNSS Receiver
DJI Phantom 4 Pro RTK UAS
Leica TS15P 1” Total Station
Leica 360° prism with bipod
2’ x 2’ Iron Cross Targets

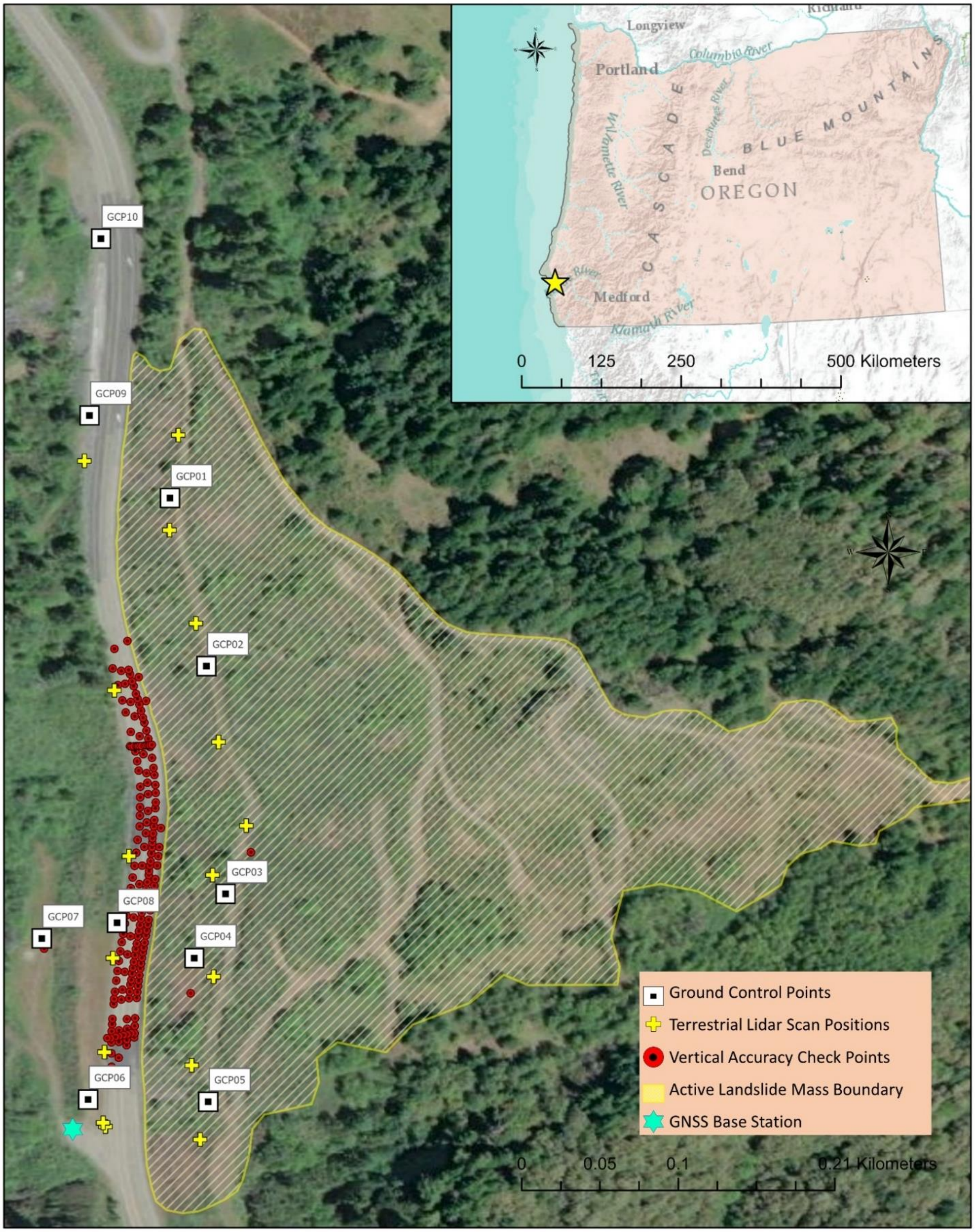

Figure 2.1. Satellite imagery and site map of the study area with GCPs marked

2.2 GNSS and Total Station Survey

GNSS was used to determine the positions of 10 ground control points (GCPs) across the site (**Figure 2.1**) and each terrestrial lidar scan station. The location of the GCPs was planned and set up based on the following considerations: even distribution throughout the proposed area; personnel safety (i.e., not located near abrupt cliffs, or near traffic); and sky visibility for both GNSS and UAS imagery data collection. For all the GNSS surveys, a minimum of 5 minutes of observations were obtained at a 1 Hz data logging rate. The coordinates of a local base station setup on the project site were computed utilizing OPUS-Projects v4.12 which referenced the base station to 6 of the nearest NGS CORS located approximately 80km, on average, from the project site. Leica Infinity v3.4 was then used to compute baseline vectors from this GNSS base station using the Post-processed Kinematic (PPK) approach.

A total station survey was performed with a Leica TS15P 1" instrument to provide a substantial number of checkpoints to validate the terrestrial lidar and UAS-SfM/MVS data. All GCPs were captured with a Leica 360° prism while all the checkpoints on the road surface were acquired via reflectorless observations due to safety concerns. A total of 180 checkpoints were observed across 7 different profiles including 4 profiles parallel to and 3 profiles perpendicular to the flow of traffic (**Figure 2.2**). The collected TS points cover the section between 200 m and 450 m of the study area due to the constraints of access to certain areas as well as safety concerns. For the same reasons, all the measurements were made with reflector-less shots rather than using prisms.

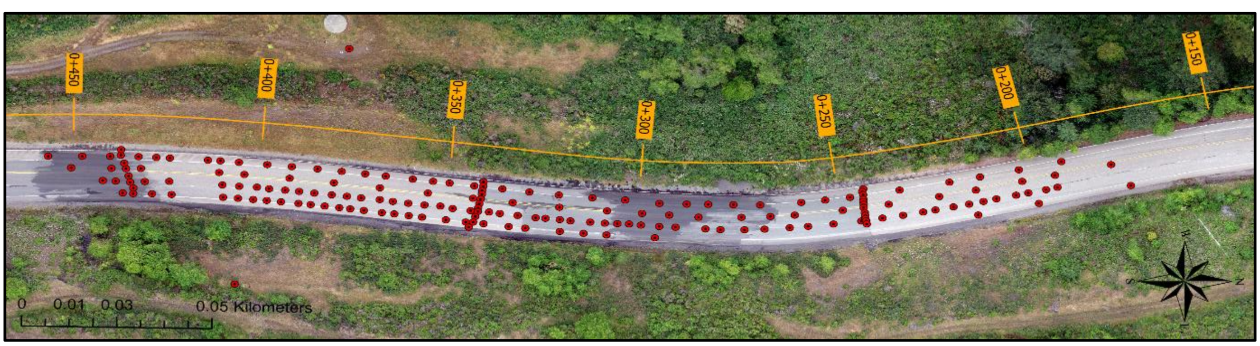

Figure 2.2. The checkpoints on the road surface surveyed by the total station.

All resulting data from the GNSS and total station surveys were combined via a least square adjustment performed in MicroSurvey Star*NET v10.0. The resulting coordinates were projected into the Oregon Coordinate Reference System (OCRS) Oregon Coast Zone and referenced to the North American Datum of 1983 (2011) epoch 2010.00. Geoid12B was used to obtain the orthometric height of the data points which are referenced to the North American Vertical Datum of 1988 (NAVD88).

2.3 Terrestrial Lidar Data

A total of 17 terrestrial lidar scans with images were collected using Riegl VZ-400 to cover the entirety of the area of interest (**Figure 2.3**). The scanner was set up on both sides of the road to increase the overall point density as well as to mitigate the occlusions caused by moving vehicles. The typical scan resolution was set to 0.05° horizontally and vertically, which can result in an approximate point spacing of 1 cm at 10 m away from the scan setup on an orthogonal surface. Note that the point spacing increases with an increasing range as well as the angle of incidence from the scanner. Therefore, it was important for the scan positions to not be spaced far from each other such that a higher point density could be achieved throughout the project area. With the GNSS receiver mounted on top of the scanner, global coordinates for each scan can be acquired and processed against the base station similarly to the GCPs, which can substantially simplify the initial alignment of the scans. The registration of the initial aligned scans was further refined using PointReg software (Olsen et al., 2011; Olsen et al., 2012b) utilizing a cloud-to-cloud matching algorithm known as ICP (Iterative Closest Point) combined with constraints to the GNSS coordinates at the scanner location. Such workflow balances the absolute geo-referencing accuracy and relative local accuracy via GNSS measurements and cloud-to-cloud matching, respectively.

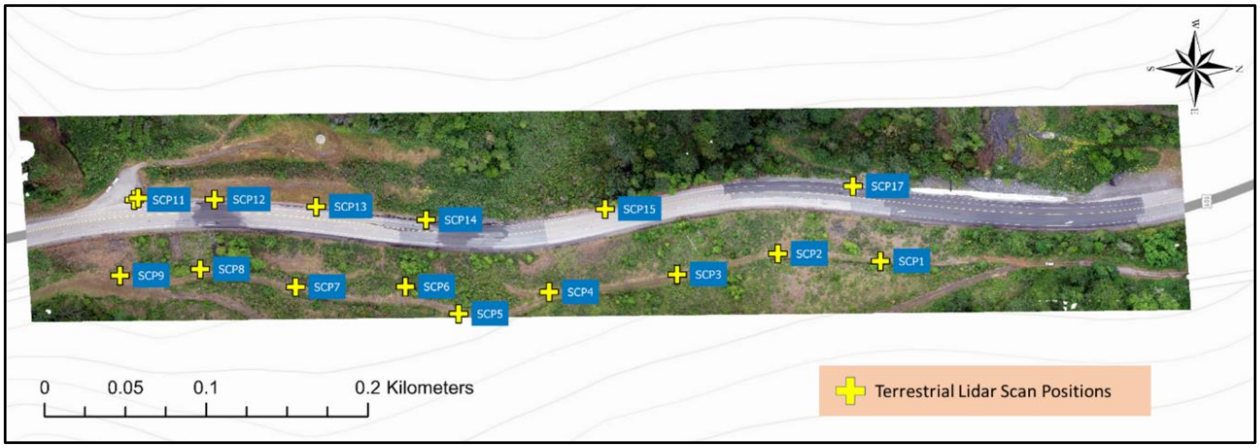

Figure 2.3. Terrestrial lidar scan positions with the project area.

2.4 UAS-SfM/MVS Data

A DJI Phantom 4 RTK drone was deployed to capture the RGB imagery for 3D reconstruction based on the SfM technique in this investigation. Special care was taken to set appropriate image acquisition parameters for the camera, including ISO range, shutter speed, aperture, and white balance (**Table 2.2**). All imagery was captured and processed in jpeg file format.

Table 2.2. UAS and camera specification

Make/Model:	**DJI P4 RTK (FC6310R)**
Resolution (pix):	5472 x 3648
Pixel Size (µm):	2.41 x 2.41
Focal Length (mm):	8.8
File Format:	.jpeg
Shutter Speed (sec):	Auto [1/100, 1/1000]
Aperture:	f/4
ISO:	Auto [100, 400]
Focus:	Auto (center)
Ground Sampling Distance (GSD)	1.4 cm per pixel
Flying Height	~48.8 m
Overlap	80%
Sidelap	80%

For SfM/MVS processing, the raw file format is generally preferred as it maintains all data acquired by the sensor while providing a high dynamic range that can decrease the total area of poorly exposed features in an image. Unfortunately, not all software/firmware supports the collection or processing of raw files. The image acquisition settings were chosen based on the previous survey of the site for topographic mapping and change detection. It is important to note that the UAS survey was not performed directly over the roadway with a low flight altitude to minimize the distraction to the drivers (Barlow et al. 2019).

The trajectory of the UAS was derived via GNSS relative positioning between the UAS and the GNSS base stations discussed in Section 2.2. The open-source GNSS processing software package, RTKLIB (Takasu & Yasuda, 2009), was used in post-processing kinematic (PPK) positioning mode to compute the remote aircraft's trajectory. Using a custom Python script, the camera positions and their covariances were extracted from the GNSS trajectory, transformed to the desired map projection, and used as input in Agisoft Metashape for SfM/MVS processing (Senogles A., 2021). Note that using the PPK GNSS positions of the acquired images reduces the need for GCPs when using SfM/MVS software, hence decreasing the total data acquisition time. The coordinates (X, Y, Z) of each photo are attained from the PPK trajectory and used to seed the SfM algorithm. Constraining the position for each photo rather than relying solely on established GCPs provides a refined position to use in the least squares bundle block adjustment to determine the remaining extrinsic (roll, pitch, yaw) and intrinsic parameters of the camera. GCPs were still used to provide the SfM software with more information to better compute the position and orientation of each image as well as the intrinsic camera parameters. The resulting 3D point cloud, cropped to the roadway, from the SfM reconstruction is shown in **Figure 2.4**.

Figure 2.4. UAS-SfM/MVS dense point cloud data representation of the highway

2.5 Point Cloud Processing

The point clouds from UAS-SfM/MVS and terrestrial laser scanning (TLS) both included a substantial amount of data off the road that was not relevant to this research. As a result, the point cloud data were cropped in CloudCompare, a commonly used open-source 3D point cloud (and triangular mesh) editing and processing software (Transtec Group, 2016).

There are a few procedures to clean up the data to remove the artificial roughness provided by DEMs. For instance, the raw point clouds include non-ground objects such as cars in traffic as an isolated cluster. Therefore, prior to creating a digital elevation model, the ground and non-ground points must be separated. This process referred to as ground filtering, can be arduous and time-consuming if performed manually due to the amount of effort required. An effective and scalable versatile ground filter based on multi-scale voxelization and smooth segments, named Vo-SmoG (Che et al., 2021) was used to accomplish the ground filtering. It is also worth noting that a better result can be achieved with additional manual cleaning.

It is also necessary to eliminate data gaps that have developed as a result of various impediments blocking the line of sight to the object of interest. These holes also may stem from portions that were captured with oblique scans when scanning near cliffs, especially in highway projects (Olsen et al., 2009). One way to reduce these data gaps is by increasing the number of scans. Fortunately, in this project, there was a sufficient number long and short-range scans for the TLS data acquisition to minimize gaps/holes in the dataset (**Figure 2.3**). As a side note, even though Riegl VZ-400 is equipped with inclination sensors that can provide the tilting angles of each setup such that the scanner is not required to be physically leveled. For long-range scans, however, it is recommended that the scanner be leveled to minimize potential errors (Silvia & Olsen, 2012). Similarly, the high overlap and sidelap percentages (80%) of the UAS mission plan help to ensure that the project area is thoroughly imaged such that the resulting UAS-SfM/MVS data has the least amount of gaps and holes.

For some areas with data gaps, the alternative method is to fill these holes by predicting the topography in those areas with the existing measurement. The RAMBO software (Olsen et. al, 2020) was used to generate 0.1 m resolution DEMs from the point clouds with data gaps filled using a windowed thin plate spline method (Olsen et. al, 2015) to provide a smooth interpolation through the data gaps based on surrounding data. RAMBO also performs a median filter to smooth out noise within a cell. Optimal results are obtained when a proper balance between modeling resolution and hole filling is struck to minimize data gaps while avoiding over-interpolation (Olsen et al., 2015).

2.6 Roughness Index Calculations

2.6.1 Profile Extraction

The pavement profiles for roughness calculation were extracted from the DEMs using python scripts for batch processing developed in ArcGIS Pro version 2.9.0 software. The primary process flowchart is depicted in the steps below (**Figure 2.5**):

1. TLS point cloud data was first georeferenced using GNSS data obtained at each setup, while the GNSS data at GCPs were used to georeferenced UAS-SfM/MVS point cloud data. Afterward, CloudCompare was used to crop the dense point cloud to the pavement surface area, followed by Vo-SmoG ground filtering that down-sampled the data and classified it into the ground and non-ground points.

2. RAMBO software was used to generate DEMs with 0.1m resolution with the function of gap-filling enabled.
3. Prospective pathways for the car wheels were manually digitized in ArcGIS Pro with longitudinal road markings as guidelines, resulting in 6 longitudinal profiles including 4 north-bound and 2 south-bound.
4. Sampling points were extracted along these 6 profiles with a fixed interval of 0.3 m (12 in.) based on the recommendations from existing studies (Chin & Olsen, 2014) and existing guidelines (ASTM E1926-08, 2021). The elevations of the sampling points were extracted from the DEMs using bilinear interpolation if needed.
5. The attribute table containing the point ID, XY coordinates, and elevation information of the sampling points was exported into a spreadsheet for generating ERD files for the subsequent analysis.
6. The IRI analyses were conducted for each longitudinal profile through the ProVAL software with ERD files as input.

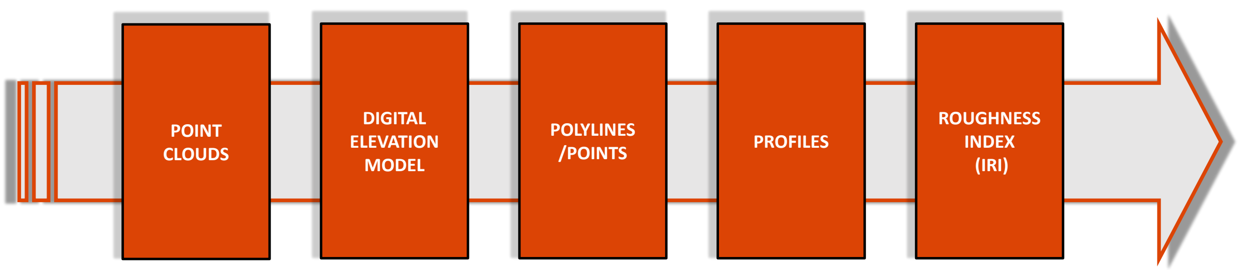

Figure 2.5. Main Workflow

2.6.2 ProVAL Computations

IRI analyses were conducted using ProVAL (Profile Viewing and Analysis) version 3.61.42. ProVAL is a software tool for viewing and analysis of longitudinal pavement profiles in a variety of ways (Transtec Group, 2016). Many pavement smoothness specifications, such as those developed by AASHTO, FHWA Federal Lands, and US DOT, cite ProVAL as the official standard analysis and reporting tool (Transtec Group, 2015).

The ProVAL software reads in ERD files, which are a standard data format for analyzing and measuring road profiles (Sayers & Karamihas, 1997). ERD files can either contain profile data in ASCII text or two 4-byte floating-point binary formats. ERD files are divided into two distinct sections: (1) the header containing basic information about the data (e.g., samples/channel, interval, storage format, unit, etc.), and (2) the data section, which stores all the profile elevations (**Figure 2.6.**). The output for each profile from the GIS extraction process was converted into an ERD file.

```
ERDFILEV2.00
    1, -1, -1, 1, 3, 0.3000000, -1,
TITLE   Track Run E1
SHORTNAMLElev.  LElev.
UNITSNAMft      m
XLABEL  Distance
XUNITS  m
END
```

Figure 2.6. Example ERD file header

The following parameters were applied in the ProVAL analysis. For each profile in both the UAS-SfM/MVS and TLS data, ProVAL's "Ride Quality" function was used with the 250 mm filter enabled for the roughness computations. This function also provides three types of ride statistical analysis: *Overall*, *Continuous*, and *Fixed Interval*. The *Continuous* analysis type was selected because it reports statistics for every sample location and simulates a ride more realistically. In addition to the IRI, which was the focus of this investigation, MRI (the Mean Roughness Index) and HRI (Half-car Roughness Index) indices can also be analyzed. A segment length of 30 m was used considering the sampling interval (0.3 m) and the number of samples for each segment. ProVAL provides two primary outputs: a spreadsheet listing the maximum IRI values for each segment related to the location as distance, and a visual graph representation of the result.

CHAPTER 3. ANALYSIS & DISCUSSION

3.1 Vertical Accuracy Assessment

In the initial step of the analysis, TS data served as the ground truth data against which our TLS and UAV-SfM/MVS data sets were compared, and both point-based and model-based comparisons were performed to check the data sets accuracy. The north side of the site (0 – 200m along the highway) was not covered because of the limited field of view as previously mentioned (**Figure 2.2**). That prevented us from making accuracy checks for the whole stretch of models.

Maintaining the same XY location of 180 total station points, the elevation values were generated from both the TLS and UAS-SfM/MVS DEMs in order to compare their vertical point base accuracy check with TS points by following standards (Authority, 1998). The statistical analysis demonstrates that the vertical accuracy from both data sources is within a few centimeters (**Table 3.1**).

Table 3.1. Summary of Vertical Accuracy (unit: meters)

	UAS-SfM/MVS	**TLS**
Average	0.017	0.035
Maximum	0.038	0.058
Minimum	-0.009	-0.007
Std. Deviation	0.008	0.014
RMSE	0.019	0.037
95% confidence	0.037	0.073

The root means square error (RMSE) (**Eq. 3.1**) computations validate the reliability of the collected data in reference to accuracy criteria.

$$\boldsymbol{RMSE_Z = \sqrt{\frac{\sum_{i=1}^{n}(Z_{data_i} - Z_{check_i})^2}{n}}} \qquad \textbf{Eq. 3.1}$$

The standard deviations of the vertical errors are around 0.01 m which, in principle, should support an IRI assessment considering the fact the bias (average error) does not affect the IRI assessment as significantly. It is also worth noting that even though TLS data is intended to be used as control data, its overall vertical accuracy is lower than that of UAS-SfM/MVS data. The following factors could lead to this situation:

- UAS-SfM/MVS used the same GCPs as the total station, which can minimize its vertical bias. Meanwhile, TLS was georeferenced with just GNSS post-processed kinematic (PPK) data collected from a receiver mounted on top of the scanner independent from the GCPs except for the shared base station. As shown in the statistical analysis, the vertical accuracy of the TLS-derived DEMs is in line with the typical accuracy of GNSS measurements.
- The smoothing process during the DEMs generation is relatively more effective in filtering the noise in the UAS-SfM/MVS point cloud partially because it typically has a more uniform point distribution than TLS which is heavily impacted by the range and angle of incidence. In the study area, there are sections where the measurements from long-range and oblique angles had to be used due to occlusions and restrictions of setup locations.
- The total station measurements were mostly obtained on or near the pavement markings where the UAS-SfM/MVS have superior performance because the high contrast provides more key points for matching in the 3D reconstruction. Although reflective markings can be captured at a longer range for the TLS compared with the pavement surface, the TLS scans can suffer from an oblique angle at a long range because the larger footprint of the laser beam can introduce more ranging errors.

3.2 DEMs Comparisons

The DEMs generated from the UAS-SfM/MVS and TLS point clouds were compared visually and quantitatively using several data products from both data sources such as the orthomosaic image, hillshades, and the DEMs difference raster (**Figure 3.1**). Closeup views of certain features will be shown in Section 3.3 which focuses on the localized analysis results.

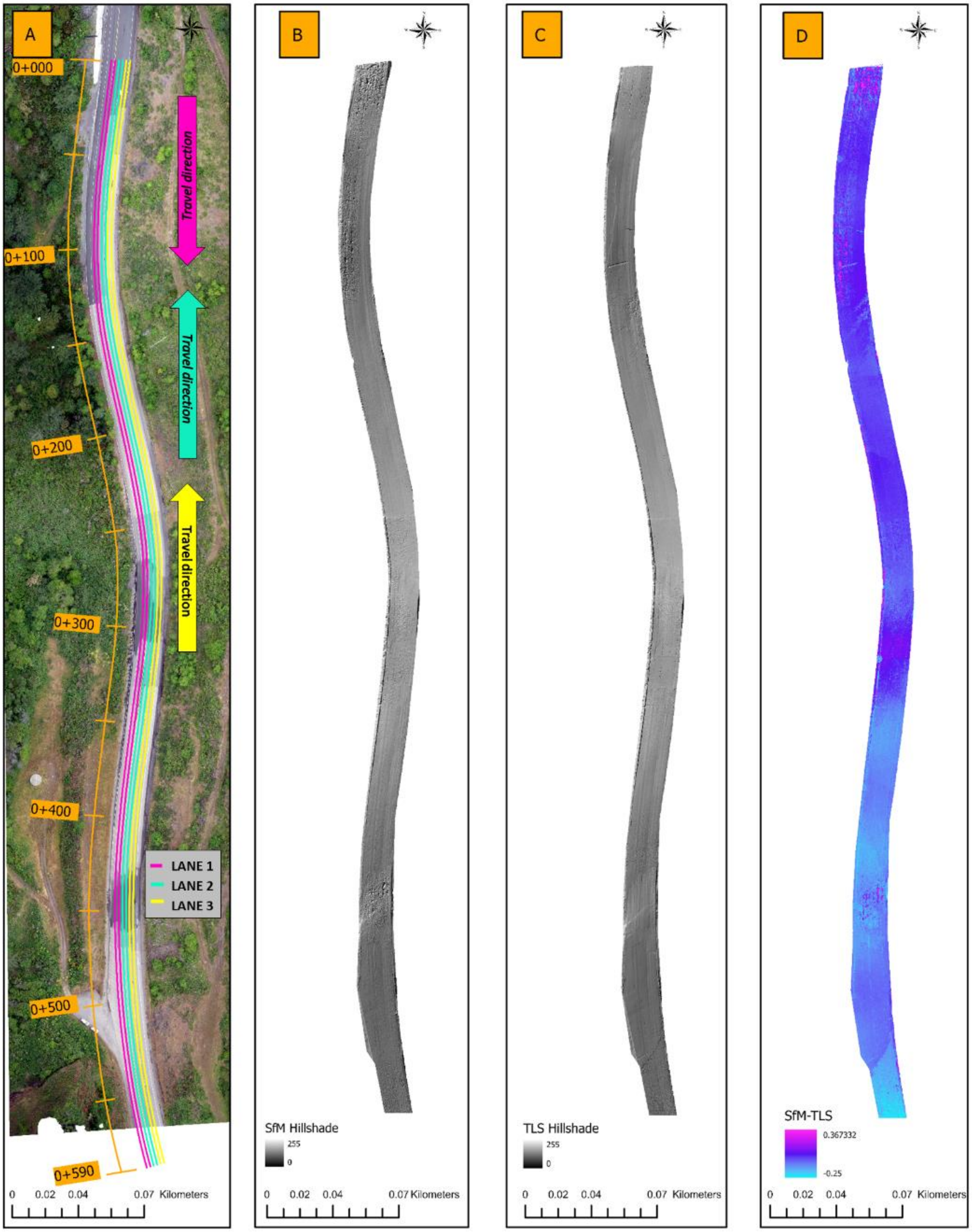

Figure 3.1. Overview of data products from TLS and UAS-SfM/MVS. A) The Orthomosaic of the pavement, B) UAS-SfM/MVS derived DEMs` hillshade map, C) TLS derived DEMs` hillshade map, D) The vertical difference UAS-SfM/MVS and DEMs data representation

The orthomosaic shows an overview of the area of interest (AOI) including three newly paved portions (**Figure 3.1.A**). Note the AOI is referenced with the local stationing starting from north to south. Between 0 and 150 m, the west side of the road (the lanes on the left on the map) is newly paved with asphalt, resulting in a very dark surface. In the same area, significant rough artifacts occur in the UAS-SfM/MVS DEMs corresponding to the darker area (**Figure 3.1.B**). On the other hand, it appears substantially smoother in the TLS hillshade map than in the UAS-SfM/MVS, only with some minor artifacts present. The artifacts in the TLS data are most likely caused by the fact that it is so close to the AOI's boundary, resulting in a much lower point density in this area. UAS-SfM/MVS, however, has adequate buffers to ensure the full coverage of the AOI. Thus, the artifacts are mostly from the lack of matching key points caused by dark and texture-less surfaces (**Figure 3.2**). This is further observed within other segments such as 250 – 350 m and 400 – 500 m along the highway the UAS-SfM/MVS behaves similarly while TLS again obtains a smooth surface (**Figure 3.1.C**), showing a strong correlation between the dark surface and rough artifacts of the UAS-SfM/MVS DEMs.

It is also worth noting that even though overall the TLS accurately reflects the geometric characteristics of the road surface regardless of the color and material of the pavement, some artifacts still occur occasionally across the site (e.g., linear artifacts near 110 m along the highway). These are mostly caused by geo-referencing and registration errors between the TLS scans due to many factors such as obliqueness, leveling errors, GNSS errors, ranging errors, lack of smooth surface serving as constraints in point cloud alignment, and so on. All the aforementioned artifacts are presented and quantified in the difference map between the UAS-SfM/MVS and TLS DEMs (**Figure 3.1.D**). In the following sections, the difference between UAS-SfM/MVS and TLS DEMs will be further analyzed quantitatively.

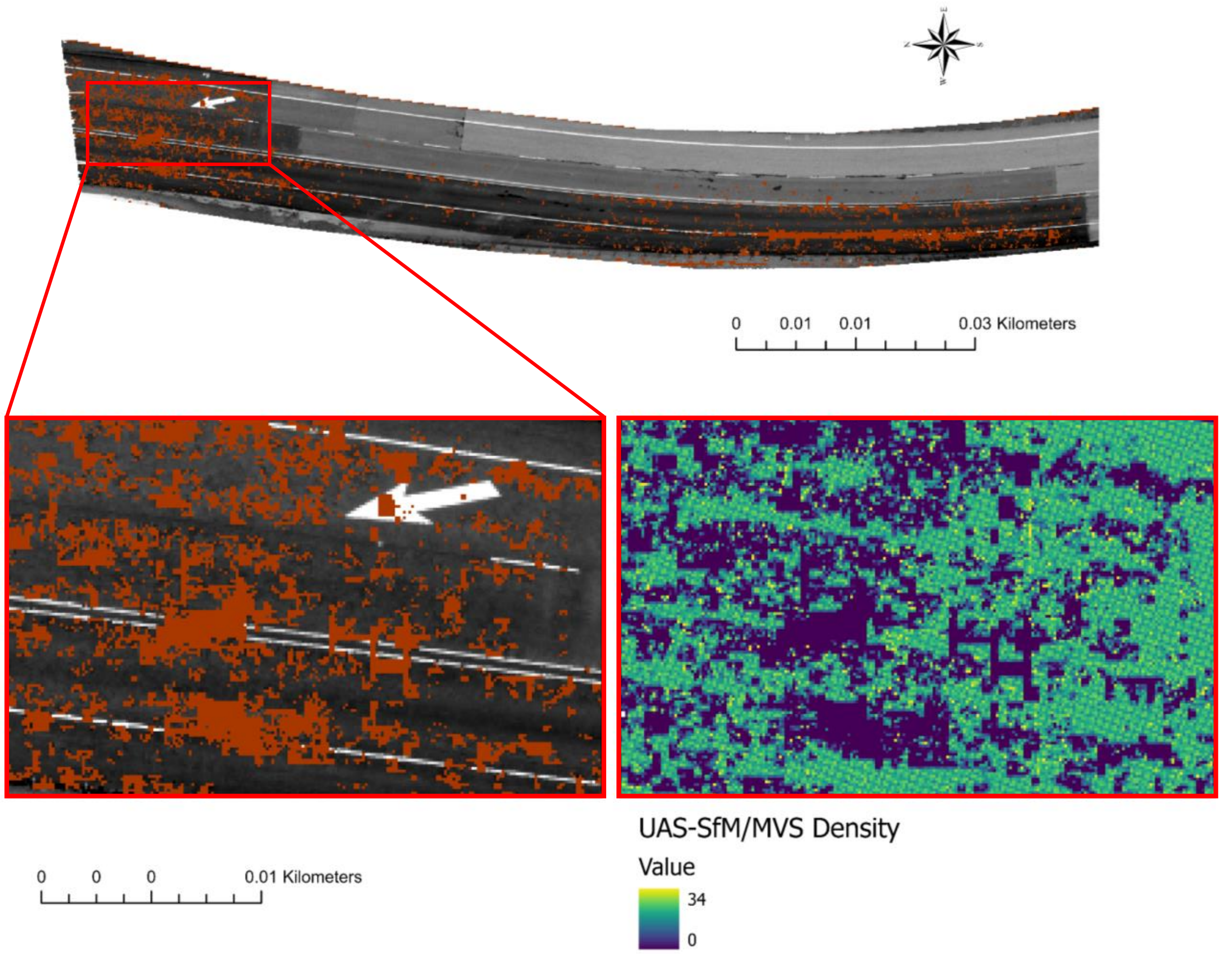

Figure 3.2. Close inspection of gaps in the UAS-SfM/MVS data where orange pixels represent interpolated data gaps and the DEMs colored by intensity.

3.3 Lane Profile and IRI Comparison

In order to further evaluate the IRI values derived from the UAS-SfM/MVS point cloud, the total station checkpoints and terrestrial lidar point cloud were also used to generate IRI values along a number of pre-defined longitudinal profiles. The IRI values from TLS and UAS-SfM/MVS were first compared against the TS measurements. Then a more comprehensive and detailed comparison and analysis were conducted to compare TLS- and UAS-SfM/MVS-derived IRI values.

3.3.1 Validation of Total Station Data

About 3500 points were produced along four parallel longitudinal profiles and their elevation was extracted from each of these three DEMs through ArcGIS pro software. Because the DEM from total station data needs to be heavily interpolated due to the relatively low spatial resolution, the elevations of the total station points were first compared against those from TLS and UAS-SfM/MVS for assessment. The RMSE for UAS-SfM/MVS and TLS is about 2 cm and 3 cm from the TS checkpoints, respectively (**Table 3.2**). These values are on par with the accuracy assessment in the previous section on the checkpoints, which validates the overall effectiveness of the total station data in producing a DEM for this task. It is also worth noting that the standard deviation, minimum, and maximum values tend to vary more due to the limited representation of the local surface variation from the total station data.

Table 3.2. The elevation difference statistics both between UAS-SfM/MVS-TS and TLS-TS (unit: meters)

	UAV-SfM/MVS-TS				**TLS-TS**			
	Lane1L	**Lane1R**	**Lane2L**	**Lane2R**	**Lane1L**	**Lane1R**	**Lane2L**	**Lane2R**
Average	-0.011	-0.011	-0.004	-0.006	-0.027	-0.027	-0.020	-0.023
Maximum	0.044	0.031	0.035	0.035	0.019	0.004	0.014	0.008
Minimum	-0.088	-0.060	-0.047	-0.095	-0.078	-0.061	-0.050	-0.064
Std. Deviation	0.019	0.011	0.015	0.010	0.015	0.012	0.012	0.012
RMSD	0.022	0.016	0.016	0.012	0.031	0.030	0.023	0.026
95% Confidence	0.043	0.032	0.031	0.024	0.061	0.058	0.046	0.051

Next, the IRI indices produced from the TS, TLS, and UAS-SfM/MVS DEMs were compared to each other (**Table 3.3**). The IRI values derived from TLS data show more consistency with the TS than those generated from UAS-SfM/MVS DEMs across different lanes (**Figure 3.3**). For example, the RMSD of IRI values obtained from UAS-SfM/MVS data on Lane 1 Right (Lane1R) is nearly three times of TLS data. Additionally, the maximum IRI and the standard deviation values for the UAS-SfM/MVS data indicate high noise levels and they also vary significantly in different lanes.

Table 3.3. IRI index difference statistics (unit: m/km=m/mm)

	UAV-SfM/MVS-TS				TLS-TS			
	Lane1L	**Lane1R**	**Lane2L**	**Lane2R**	**Lane1L**	**Lane1R**	**Lane2L**	**Lane2R**
Average	1.2	3.1	1.7	3.1	-0.5	0.7	-0.4	1.2
Maximum	7.6	9.7	18.1	14.5	4.0	3.8	3.5	4.2
Minimum	-3.3	-0.8	-3.2	-1.2	-4.4	-2.2	-4.2	-1.6
Std. Deviation	3.1	3.1	3.2	2.6	2.3	1.2	2.2	1.6
RMSD	3.3	4.4	3.6	4.0	2.4	1.4	2.2	2.0
95% Confidence	6.6	8.7	7.2	7.9	4.6	2.8	4.4	3.8

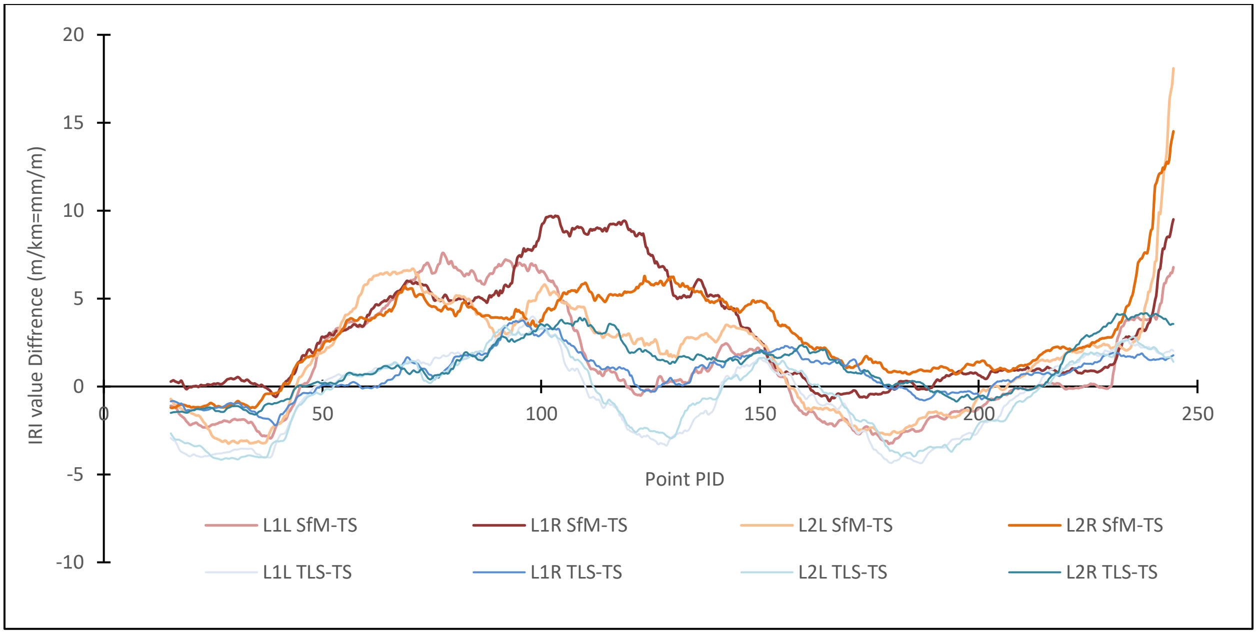

Figure 3.3. Differences between UAS-SfM/MVS-TS TLS-TS derived IRI values diagram

3.3.2 Comparison between UAS-SfM/MVS and TLS

Presented as in the statistical analysis, the deviations observed across all profiles are very consistent where the average difference, standard deviation, and RMS of the differences are around 0.01 m, 0.02 m, and 0.03 m, respectively. (**Table 3.4**). As shown in the statistical analysis, the deviations observed across all profiles are very consistent where the average difference, standard deviation, and RMS of the differences are around 0.01 m, 0.02 m, and 0.03 m, respectively. However, it is worth noting that the maximum and minimum difference between the two models shows substantially greater discrepancies, likely due to the dark and texture-less nature of the surface resulting in poorer performance of the UAS-SfM/MVS data near the landslide boundaries or areas of localized failure.

Table 3.4. Elevation difference analysis between UAS-SfM/MVS and TLS data (unit: meters)

	Lane1_L	Lane1_R	Lane2_L	Lane2_R	Lane3_L	Lane3_R
Minimum	-0.137	-0.135	-0.138	-0.128	-0.089	-0.142
Maximum	0.059	0.055	0.054	0.063	0.061	0.077
Median	0.010	0.009	0.009	0.008	0.008	0.009
Average	0.011	0.011	0.012	0.011	0.011	0.011
Std. Deviation	0.021	0.022	0.021	0.022	0.021	0.022
RMSD	0.029	0.027	0.027	0.028	0.026	0.028

Later, IRI values were computed at distinct intervals along each profile from UAS-SfM/MVS and TLS data. Based on the IRI values derived from TLS data, the average IRI values are relatively consistent across all profiles and range from 3.9 to 4.7 m/km which is expected for most parts of the pavement. However, the average IRI values from UAS-SfM/MVS data have significantly more variations and range from 7.5 to 11.4 m/km. Additionally, the IRI values from UAS-SfM/MVS data are consistently higher than TLS data, which indicates that the road surface in UAS-SfM/MVS is rougher than the TLS DEMs. More noticeably, the difference between the profile elevations is clearly amplified and propagated to the IRI calculations, especially for UAS-SfM/MVS data. For example, the maximum IRI values computed from UAS-SfM/MVS data for all profiles range from 45.5 to 79.6 m/km, which shows tremendous roughness. Nonetheless, despite some variations in the maximum IRI values in TLS data, it is much more consistent compared to UAS-SfM/MVS data (ranging from 10.3 to 16.5 m/km), which can be largely explained by some localized differences between lanes and profiles.

Then, the differences in IRI computed from TLS and UAS-SfM/MVS datasets are further reported statically (**Table 3.5**) while **Table 3.6** shows how the elevation differences in the profiles affect the IRI values. The average difference between the IRI values ranges between 2.9 and 7.6 m/km for each profile, which shows a clear bias in using UAS-SfM/MVS data to estimate the IRI values. The RMSD also considers both the bias and variation in the difference of

IRI value and it ranges from 9.0 to 13.7 m/km. Considering the typical scale of the IRI measures (**Figure 1.1**), the TLS-derived IRI indicates that the road is "Older Pavement" overall with some sections that are "New Pavements" and "Damaged Pavements". On the other hand, the IRI assessment from UAS-SfM/MVS data shows that the road is "Damaged Pavements" on average with some "New Pavements" and some "Rough Unpaved Roads". In this instance, the TLS-derived IRI values more accurately depict the road surface condition.

Table 3.5. Statistical summary of IRI values for each profile from TLS and UAS-SfM/MVS data

(m/km)	**Lane1_Left**	**Lane1_Right**	**Lane2_Left**	**Lane2_Right**	**Lane3_Left**	**Lane3_Right**
			Terrestial Lidar Data IRI (m/km)			
Minimum	0.8	1.1	1.0	1.2	1.3	1.0
Maximum	11.1	11.0	10.3	14.1	11.9	16.5
Median	3.5	3.8	3.5	3.6	3.8	3.8
Average	3.9	4.1	3.8	4.3	4.4	4.6
			UAS-SfM/MVS Data IRI (m/km)			
Mimimum	1.9	2.2	2.0	2.0	1.8	2.1
Maximum	77.6	68.2	79.6	45.5	65.4	71.2
Median	7.0	6.5	6.4	4.5	4.2	4.6
Average	11.4	10.6	9.0	7.9	7.5	7.6

Table 3.6. Statistical summary of the IRI value differences (unit: m/km)

(m/km)	**Lane1_Left**	**Lane1_Right**	**Lane2_Left**	**Lane2_Right**	**Lane3_Left**	**Lane3_Right**
Minimum	-3.1	-6.5	-5.3	-10.8	-9.8	-13.8
Maximum	69.7	58.6	69.6	41.3	57.8	67.5
Median	2.8	1.9	2.4	1.7	1.2	1.0
Average	7.6	6.5	5.1	3.6	3.1	2.9
Std. Deviation	11.4	11.5	9.1	8.3	8.6	10.2
RMSD	13.7	13.2	10.5	9.0	9.1	10.6

To further analyze how the IRI difference between TLS and UAS-SfM/MVS data behave and vary across the site, the difference between datasets is plotted in a graph (**Figure 3.4**). First of all, it is worth noting that some of the large discrepancies from the beginning and end of the profiles could be a result of the artifacts near the boundary from both the data and ProVAL software. Aside from those areas, most of the larger discrepancies occur in three zones whereas the difference in other areas is generally within 3 m/km, which shows that the IRI assessments from TLS and UAS-SfM/MVS are on par with each other.

Then for those three zones (i.e., Zone-A, Zone-B, and Zone-C) with large differences, a more detailed analysis is carried out. As shown in the close-up views of the three zones (**Figure 3.5**), they all feature large roughness caused by data gaps and errors, particularly where the recently paved areas are located with darker surfaces in comparison to other parts. To further quantify the impact of such texture-less and dark surfaces on the IRI assessment, the research team extracted these subsections from the profiles and analyzed the difference in both elevations and IRI values statistically (**Table 3.7** and **Table 3.8**).

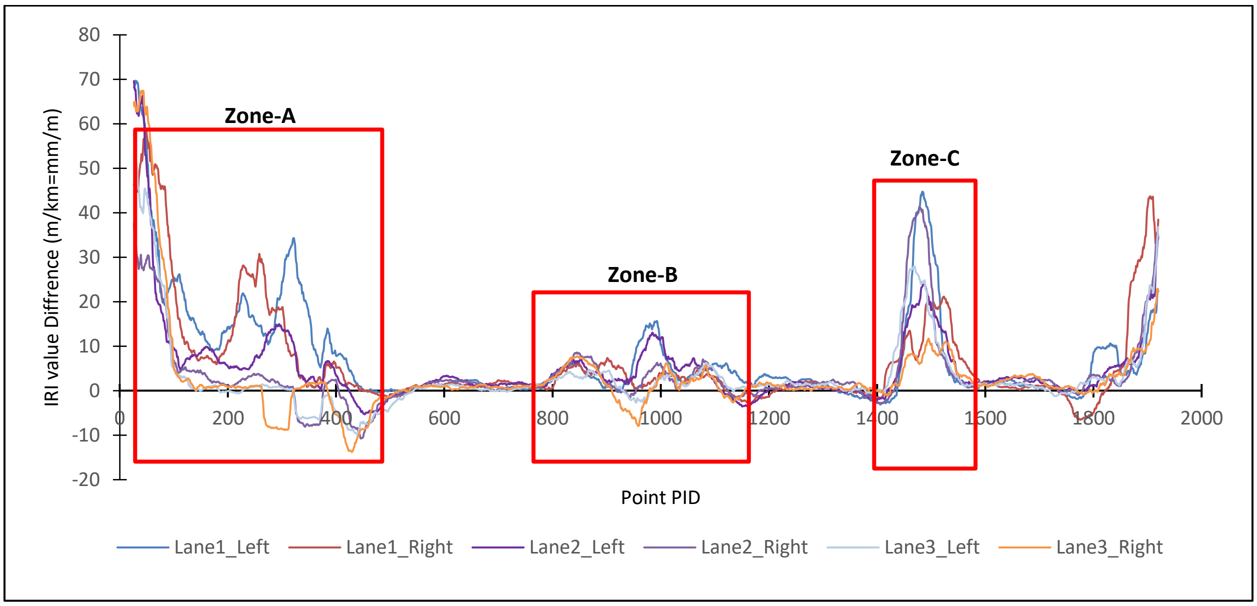

Figure 3.4. Differences between UAS-SfM/MVS and TLS-derived IRI values diagram

Based on the statistical analysis, large vertical variations were observed in Zone A and Zone C, whereas there are no notable differences in vertical data in Zone B. The IRI difference in these zones follows the same trend in general. For Zone A and Zone B, the large discrepancy can be largely explained by the higher noise level and more data gaps in those areas. For Zone B, however, despite the fact that the average, standard deviation, and RMSD of the elevations from UAS-SfM/MVS data are on par with those of the TLS data, the UAS-SfM/MVS data still provides a higher estimation of the IRI values. The reduction in artifacts in Zone B can be explained by 1) Zone B has the smallest patch of very dark asphalt pavement, and 2) the irregular shape of the patch provides relatively more contrast to the image which is essential for the 3D reconstruction process. That being said, there are still many small data gaps in this section and the gap-filling algorithms can cope with this to generate reasonable DEMs. Besides, given the complexity of the surface itself, the assumptions made in the gap-filling and smoothing approaches can no longer accurately predict the actual surface characteristics.

Figure 3.5. Close-up views of the zones with new asphalt pavement.

Table 3.7. The elevation difference between UAS-SfM/MVS and TLS by zones (unit: meters)

	(m)	Lane1_L	Lane1_R	Lane2_L	Lane2_R	Lane3_L	Lane3_R
Zone A	**Minimum**	-0.137	-0.135	-0.138	-0.128	-0.076	-0.123
	Maximum	0.035	0.029	0.043	0.042	0.036	0.077
	Median	0.003	0.002	0.003	0.001	0.001	0.000
	Average	-0.001	-0.001	0.001	-0.001	-0.001	-0.004
	Std. Deviation	0.023	0.019	0.017	0.018	0.016	0.019
	RMSD	0.023	0.019	0.017	0.018	0.016	0.019
Zone B	**Minimum**	-0.021	-0.031	-0.024	-0.027	-0.023	-0.026
	Maximum	0.038	0.032	0.039	0.031	0.026	0.034
	Median	0.010	0.008	0.009	0.010	0.010	0.011
	Average	0.007	0.006	0.007	0.007	0.007	0.008
	Std. Deviation	0.014	0.013	0.012	0.011	0.011	0.011
	RMSD	0.015	0.014	0.014	0.013	0.013	0.014
Zone C	**Minimum**	-0.086	-0.025	-0.022	-0.067	-0.046	-0.001
	Maximum	0.059	0.055	0.050	0.063	0.061	0.049
	Median	0.032	0.033	0.032	0.032	0.029	0.029
	Average	0.027	0.032	0.031	0.028	0.026	0.030
	Std. Deviation	0.020	0.011	0.011	0.016	0.016	0.008
	RMSD	0.034	0.034	0.034	0.033	0.031	0.032

Table 3.8. IRI value difference UAS-SfM/MVS and TLS by zones (unit: m/km)

	(m/km)	Lane1_L	Lane1_R	Lane2_L	Lane2_R	Lane3_L	Lane3_R
Zone A	**Minimum**	3.7	0.8	-1.2	-8.3	-8.8	-13.8
	Maximum	69.5	58.3	69.5	37.7	57.8	67.8
	Median	16.3	11.1	7.6	2.4	0.6	0.8
	Average	20.2	17.8	12.0	5.0	5.1	7.0
	Std. Deviation	14.1	15.9	14.8	10.3	14.6	20.3
	RMSD	24.6	23.9	19.1	11.4	15.4	21.4
Zone B	**Minimum**	0.2	-1.0	-1.8	-1.9	-2.6	-7.7
	Maximum	15.6	7.3	13.0	8.5	6.3	7.6
	Median	4.4	3.4	4.8	3.6	3.0	2.4
	Average	5.1	3.3	4.9	3.5	2.5	1.8
	Std. Deviation	3.8	1.8	3.3	2.6	2.1	3.7
	RMSD	6.4	3.7	5.9	4.4	3.2	4.1
Zone C	**Minimum**	-2.7	1.4	-2.0	-2.4	-0.4	-1.3
	Maximum	44.8	21.4	24.2	41.3	27.7	11.8
	Median	5.7	9.2	9.6	7.1	8.6	6.4
	Average	14.3	11.2	10.1	13.6	11.4	5.8
	Std. Deviation	16.1	5.9	7.8	15.1	9.3	3.7
	RMSD	21.5	12.7	12.7	20.3	14.7	6.8

3.3.3 Correlation between DEM and IRI Deviation

The statistical metrics used in determining the deviation of the DEM models were also examined with the RMSD of IRI values to determine the effectiveness of predicting the accuracy of IRI calculation with the point cloud or DEM accuracy (**Figure 3.6**). It is worth mentioning that for all the metrics, the samples in Zone B are clustered together while the other two zones are more scattered. This is because the color of the paved patch in this zone is more uniform with the existing pavement surface. The size of the new patch in that section is also considerably smaller as against the patches in the other two zones.

First of all, the IRI-RMSD has no clear correlation with the median (**Figure 3.6.D**) or average errors in the DEMs derived from UAS-SfM/MVS point clouds (**Figure 3.6.E**). This aligns with the fact that IRI is a metric describing the local variation of the surface, whereas those two metrics mostly present the global bias in the UAS-SfM/MVS data. Simply moving the entire dataset vertically to account for a bias will not result in any additional error in the IRI. For the same reason, the metric considering the bias in the data, elevation RMSD, does not provide a significant correlation either. It is slightly better than the median and average errors because the local variation also plays a role in such a metric.

Then we tested both the standard deviation and range of the errors which describe the local variation of the surface. A moderate correlation can be observed from both metrics (**Figure 3.6.A** & **Figure 3.6.C**). The range is computed as the difference between the maximum and minimum errors. Typically, such a metric can be sensitive to large errors or blunders, which makes it less reliable. However, during the 3D reconstruction in the SfM process and DEMs production stage, the most significant errors/blunders were filtered from the data. In addition, ProVAL also applies a moving low pass filter (with a 250 mm window) to the longitudinal profile to simulate the tire encircling effect by averaging values of nearby points. As a result, the standard deviation of the errors is very small and ranges from less than 0.01m to 0.025 m (**Figure 3.6.A**). On the other hand, thanks to the aforementioned smoothing process, the range of errors is much less sensitive and has a good correlation with IRI RMSD with a coefficient of 0.75 (**Figure 3.6.C**), the highest among all the metrics tested. In summary, the range of errors observed in the DEMs derived from UAS-SfM/MVS point clouds is the better indicator of the accuracy of the IRI assessment.

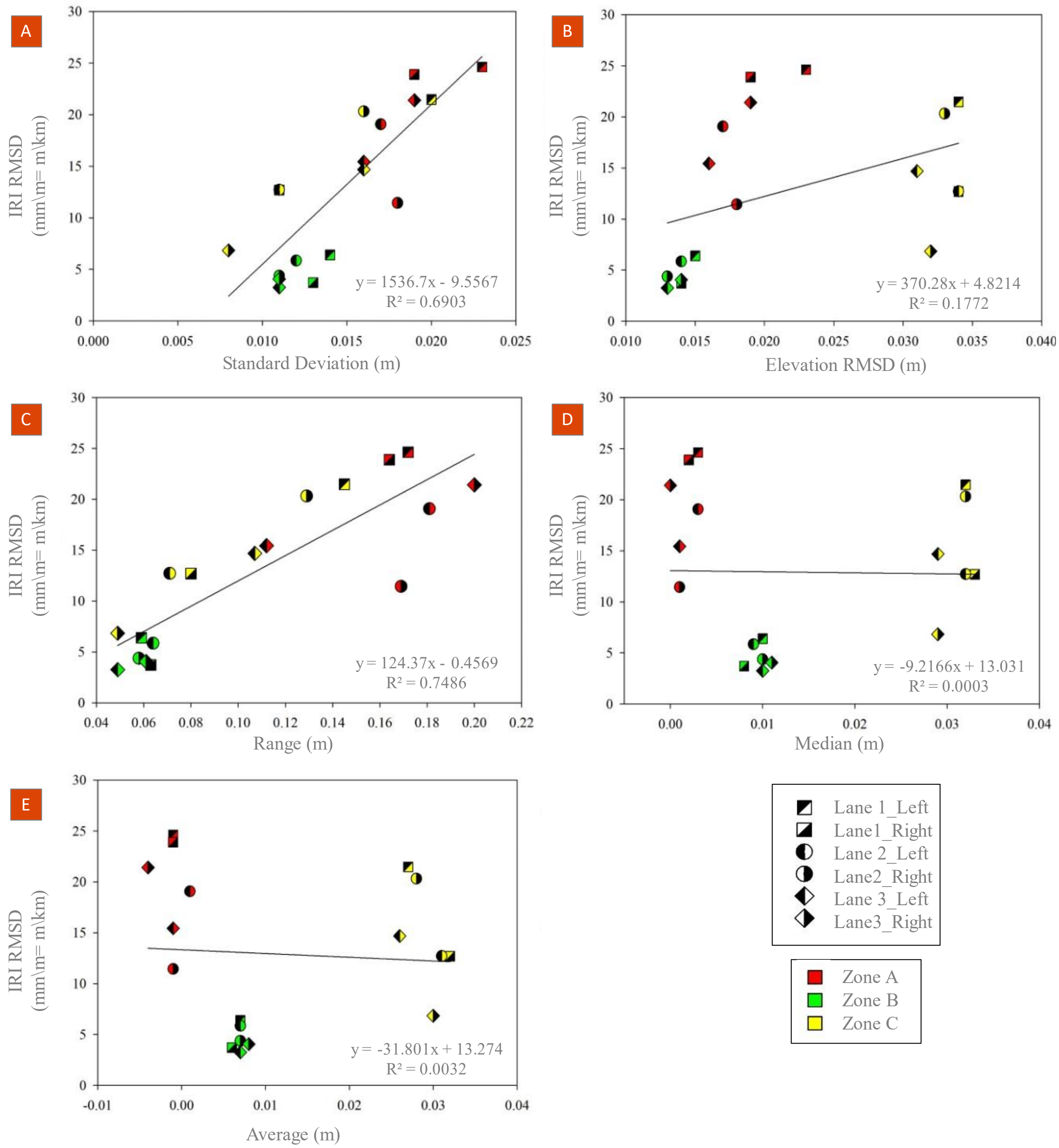

Figure 3.6. Correlation between statistical metrics and IRI RMSD (unit: m/km).

CHAPTER 4. CONCLUSION & RECOMMENDATION

This research developed a framework for collecting and processing UAS-SfM/MVS data to extract pavement information and examined the feasibility of employing UAS-derived point clouds to evaluate pavement roughness. A rigorous accuracy assessment and analysis were then conducted. First, the research team evaluated the absolute accuracy of the UAS-SfM/MVS DEMs against the total station survey including where the RMSE is 0.019 m among 180 checkpoints along the study area. Next, the UAS-SfM/MVS DEMs were further compared to the DEMs generated from TLS data along a number of profiles and the RMSDs were consistently under 0.03 m. Furthermore, the differences in IRI values along these profiles from TLS and UAS-SfM/MVS data were compared.

Based on these analyses, the following observations are made when using UAS-SfM/MVS data for pavement smoothness evaluation:

- UAS provides additional data on surrounding features, as expected from an air-based vehicle with a large field of view; thereby, the collected data can be used for more comprehensive analysis and other applications. This can also help provide more context to the pavement roughness information.
- It is challenging for the SfM technique to reconstruct 3D information on dark and texture-less surfaces such as newly paved asphalt. The results show that the dark and texture-less surface (e.g., asphalt) can result in significant vertical errors and data gaps, leading to unreliable IRI readings. On the other hand, for other parts of the road surface in a lighter color, the UAS-SfM/MVS data slightly overestimates the roughness (generally within 3 m/km) compared to the TLS data.
- Relatively small elevation derivations may have a massive effect on the IRI analysis. A localized analysis is recommended if abnormal IRI values are spotted.

Therefore, the research concludes that UAS-SfM/MVS can be a suitable technique for road surface roughness assessment with some restrictions of the color of the pavement due to its newness.

The following tasks could be tackled in future research:

- Test if the artifacts in the UAS-SfM/MVS data can be mitigated by different flight planning and data acquisition strategies.
- Compare the UAS-SfM/MVS point clouds generated from different software and settings, as well as their derivative roughness assessment results.
- Investigate the impact of different approaches and parameters in generating DEMs and interpolations.

REFERENCES

Alhasan, A., Younkin, K., & White, D. J. (2015). *Comparison of roadway roughness derived from LIDAR and SFM 3D point clouds* (No. InTrans Project 15-543). Iowa State University. Institute for Transportation.

Agüera-Vega, F., Carvajal-Ramírez, F., & Martínez-Carricondo, P. (2017). Assessment of photogrammetric mapping accuracy based on variation ground control points number using unmanned aerial vehicle. *Measurement*, *98*, 221-227.

ASTM E1926-08. (Reapproved 2021). Standard practice for computing international roughness index of roads from longitudinal profile measurements. *West Conshohocken, PA: ASTM International*.

Authority, T. V. (1998). Geospatial Positioning Accuracy Standards Part 3: National Standard for Spatial Data Accuracy. *National Aeronautics and Space Administration: Virginia, NV, USA*.

Barbarella, M., De Blasiis, M. R., & Fiani, M. (2019). Terrestrial laser scanner for the analysis of airport pavement geometry. *International Journal of Pavement Engineering*, *20*(4), 466-480.

Barlow, Z., Jashami, H., Sova, A., Hurwitz, D. S., & Olsen, M. J. (2019). Policy processes and recommendations for Unmanned Aerial System operations near roadways based on visual attention of drivers. *Transportation research part C: emerging technologies*, *108*, 207-222.

Bennett, C. R., De Solminihac, H., & Chamorro, A. (2006). Data collection technologies for road management.

Bolkas, D. (2019). Assessment of GCP number and separation distance for small UAS surveys with and without GNSS-PPK positioning. *Journal of Surveying Engineering*, *145*(3), 04019007.

Che, E., Jung, J., & Olsen, M. J. (2019). Object recognition, segmentation, and classification of mobile laser scanning point clouds: A state of the art review. *Sensors*, *19*(4), 810.

Che, E., Senogles, A., & Olsen, M. J. (2021). Vo-SmoG: A Versatile, Smooth Segment-based Ground Filter for Point Clouds via Multi-scale Voxelization. *ISPRS Annals of the Photogrammetry, Remote Sensing and Spatial Information Sciences, 8*, 59-66.

Chin, A., & Olsen, M. J. (2014). Evaluation of technologies for road profile capture, analysis, and evaluation. *Journal of Surveying Engineering*, *141*(1), 04014011.

Cruz, O. G. D., Mendoza, C. A., & Lopez, K. D. (2021, July). International Roughness Index as Road Performance Indicator: A Literature Review. In *IOP Conference Series: Earth and Environmental Science* (Vol. 822, No. 1, p. 012016). IOP Publishing.

De Blasiis, M. R., Di Benedetto, A., & Fiani, M. (2020a). Mobile laser scanning data for the evaluation of pavement surface distress. *Remote Sensing, 12*(6), 942.

De Blasiis, M. R., Di Benedetto, A., Fiani, M., & Garozzo, M. (2020b). Assessing of the road pavement roughness by means of LiDAR technology. *Coatings*, *11*(1), 17.

Dobson, R. J., Brooks, C., Roussi, C., & Colling, T. (2013, May). Developing an unpaved road assessment system for practical deployment with high-resolution optical data collection using a helicopter UAV. In *2013 International Conference on Unmanned Aircraft Systems (ICUAS)* (pp. 235-243). IEEE.

Elghriany, A., Yi, P., Liu, P., & Yu, Q. (2016). Investigation of the effect of pavement roughness on crash rates for rigid pavement. *Journal of Transportation Safety & Security*, *8*(2), 164-176.

Fakhri, M., Karimi, S. M., & Barzegaran, J. (2021). Predicting international roughness index based on surface distresses in various climate and traffic conditions using laser crack measurement system. *Transportation Research Record*, *2675*(11), 397-412.

Fonstad, M. A., Dietrich, J. T., Courville, B. C., Jensen, J. L., & Carbonneau, P. E. (2013). Topographic structure from motion: a new development in photogrammetric measurement. *Earth surface processes and Landforms*, *38*(4), 421-430.

Greenwood, W. W., Lynch, J. P., & Zekkos, D. (2019). Applications of UAVs in civil infrastructure. *Journal of infrastructure systems*, *25*(2), 04019002.

Hurwitz, D. S., Olsen, M. J., & Barlow, Z. (2018). *Driving Distraction Due to Drones* (No. FHWA-OR-RD-18-12). Oregon. Dept. of Transportation. Research Section.

Iglhaut, J., Cabo, C., Puliti, S., Piermattei, L., O'Connor, J., & Rosette, J. (2019). Structure from motion photogrammetry in forestry: A review. *Current Forestry Reports*, *5*(3), 155-168.

Inzerillo, L., Di Mino, G., & Roberts, R. (2018). Image-based 3D reconstruction using traditional and UAV datasets for analysis of road pavement distress. *Automation in Construction*, *96*, 457-469.

Javadnejad, F., Slocum, R. K., Gillins, D. T., Olsen, M. J., & Parrish, C. E. (2021). Dense point cloud quality factor as proxy for accuracy assessment of image-based 3D reconstruction. *Journal of Surveying Engineering*, *147*(1), 04020021.

Karamihas, S. (2021). *Improvement of inertial profiler measurements of urban and low-speed roadways* (Doctoral dissertation).

Lee, M. H., & Chou, C. P. (2010). Laboratory method for inertial profiler verification. *Journal of the Chinese Institute of Engineers*, *33*(4), 617-627.

Liao, Y., & Wood, R. L. (2020). Discrete and Distributed Error Assessment of UAS-SfM Point Clouds of Roadways. *Infrastructures*, *5*(10), 87.

Loizos, A., & Plati, C. (2008). An alternative approach to pavement roughness evaluation. *International Journal of Pavement Engineering*, *9*(1), 69-78.

Louhghalam, A., Akbarian, M., & Ulm, F.-J. (2015). Roughness-induced pavement–vehicle interactions: key parameters and impact on vehicle fuel consumption. *Transportation Research Record, 2525*(1), 62-70.

Múčka, P. (2017). International Roughness Index specifications around the world. *Road Materials and Pavement Design, 18*(4), 929-965.

Nappo, N., Mavrouli, O., Nex, F., van Westen, C., Gambillara, R., & Michetti, A. M. (2021). Use of UAV-based photogrammetry products for semi-automatic detection and classification of asphalt road damage in landslide-affected areas. *Engineering geology, 294,* 106363.

Olsen, M. J., Johnstone, E., Driscoll, N., Ashford, S. A., & Kuester, F. (2009). Terrestrial laser scanning of extended cliff sections in dynamic environments: Parameter analysis. *Journal of Surveying Engineering, 135*(4), 161-169.

Olsen, M. J., Johnstone, E., Kuester, F., Driscoll, N., & Ashford, S. A. (2011). New automated point-cloud alignment for ground-based light detection and ranging data of long coastal sections. *Journal of Surveying Engineering, 137*(1), 14-25.

Olsen, M. J., & Chin, A. (2012a). *Inertial and inclinometer based profiler repeatability and accuracy using the IRI model* (No. FHWA-OR-RD-13-03). Oregon. Dept. of Transportation.

Olsen, M. J., Butcher, S., & Silvia, E. P. (2012b). Real-time change and damage detection of landslides and other earth movements threatening public infrastructure.

Olsen, M. J. (2013). *Guidelines for the use of mobile LIDAR in transportation applications* (Vol. 748): Transportation Research Board.

Olsen, M. J., Wartman, J., McAlister, M., Mahmoudabadi, H., O'Banion, M. S., Dunham, L., & Cunningham, K. (2015). To fill or not to fill: sensitivity analysis of the influence of resolution and hole filling on point cloud surface modeling and individual rockfall event detection. *Remote Sensing, 7*(9), 12103-12134.

Olsen, M., Massey, C., Leschinsky, B., Senogles, A., & Wartman, J. (2020). *Predicting Seismic-Induced Rockfall Hazard for Targeted Site Mitigation* (No. FHWA-OR-RD-21-06). Oregon Department of Transportation. Research Section.

Olsen, M. J., Leshchinsky, B. A., Senogles, A., Herrmann, J., & Allan, J. (2022). *Coastal Landslide and Sea Cliff Retreat Monitoring for Climate Change Adaptation and Targeted Risk Assessment* (No. FHWA-OR-RD-22-13). Oregon Department of Transportation. Research Section.

Ong, G. P. R., Noureldin, S., & Sinha, K. C. (2010). Automated pavement condition data collection quality control, quality assurance, and reliability.

Prosser-Contreras, M., Atencio, E., Muñoz La Rivera, F., & Herrera, R. F. (2020). Use of unmanned aerial vehicles (UAVs) and photogrammetry to obtain the International roughness Index (IRI) on roads. *Applied Sciences*, *10*(24), 8788.

Radović, N., Jokanović, I., Matić, B., & Šešlija, M. (2016). A measurement of roughness as indicator of road network condition–case study Serbia. *Technical Gazette*, *23*(3).

Ragnoli, A., De Blasiis, M. R., & Di Benedetto, A. (2018). Pavement distress detection methods: A review. *Infrastructures*, *3*(4), 58.

Romero-Chambi, E., Villarroel-Quezada, S., Atencio, E., & Muñoz-La Rivera, F. (2020). Analysis of optimal flight parameters of unmanned aerial vehicles (UAVs) for detecting potholes in pavements. *Applied Sciences*, *10*(12), 4157.

Saad, A. M., & Tahar, K. N. (2019). Identification of rut and pothole by using multirotor unmanned aerial vehicle (UAV). *Measurement, 137*, 647-654.

Sayers, M. W. (1986). *Guidelines for conducting and calibrating road roughness measurements*. University of Michigan, Ann Arbor, Transportation Research Institute.

Sayers, M. W. (1989). Two quarter-car models for defining road roughness: IRI and HRI. *Transportation Research Record*, (1215).

Sayers, M. W. (1995). On the calculation of international roughness index from longitudinal road profile. *Transportation Research Record*, (1501).

Sayers, M. W. (1998). *The little book of profiling: basic information about measuring and interpreting road profiles*. University of Michigan, Ann Arbor, Transportation Research Institute.

Sayers, M. W., & Karamihas, S. M. (1997). *ERD file format for storage and analysis of road profiles*. University of Michigan, Ann Arbor, Transportation Research Institute.

Schnebele, E., Tanyu, B., Cervone, G., & Waters. (2015). Review of remote sensing methodologies for pavement management and assessment. *European Transport Research Review, 7*(2), 1-19.

Senogles, A. (2021). UAS Trajectory processing using RTKLIB for Agisoft Metashape. [accessed 2021 July 16]. https://github.com/asenogles/uas-trajectory#uas-trajectory-processing-using-rtklib-for-agisoft-metashape

Senogles, A., Olsen, M. J., & Leshchinsky, B. (2022). SlideSim: 3D Landslide Displacement Monitoring through a Physics-Based Simulation Approach to Self-Supervised Learning. *Remote Sensing*, *14*(11), 2644.

Shan, J., & Toth, C. K. (2018). *Topographic laser ranging and scanning: principles and processing*: CRC press.

Silvia, E. P., & Olsen, M. J. (2012). To level or not to level: Laser scanner inclination sensor stability and application. *Journal of Surveying Engineering, 138*(3), 117-125.

Simpson, C. H. (2018). A multivariate comparison of drone-based structure from motion and drone-based lidar for dense topographic mapping applications.

Slocum, R. K. & Parrish, C. E. (2017) 'Simulated Imagery Rendering Workflow for Accuracy Assessments UAS-based Photogrammetric 3D Reconstruction Accuracy Assessments', *Remote Sensing*, 9(4), p. 396. doi: 10.3390/rs9040396.

Smith, K. D., & Ram, P. (2016). *Measuring and Specifying Pavement Smoothness:[techbrief]* (No. FHWA-HIF-16-032). United States. Federal Highway Administration.

Takasu, T., & Yasuda, A. (2009, November). Development of the low-cost RTK-GPS receiver with an open source program package RTKLIB. In *International symposium on GPS/GNSS* (Vol. 1). International Convention Center Jeju Korea.

Tan, Y., & Li, Y. (2019). UAV photogrammetry-based 3D road distress detection. *ISPRS International Journal of Geo-Information, 8*(9), 409.

Thomas, F. (2021). *Can the method for calculating the International Roughness Index used by the company Infrafocus be certified according to Dutch regulations?* (University of Twente).

Transtec Group. (2015). ProVAL Software: View and Analyze Pavement Profiles. *ProVAL Website.* Retrieved from https://www.thetranstecgroup.com/portfolio-items/ProVAL-software-view-and-analyze-pavement-profiles/

Transtec Group. (2016). ProVAL user's guide, version 3.6. In: The Transtec Group Austin, TX.

Varbla, S., Ellmann, A., & Puust, R. (2021). Centimetre-range deformations of built environment revealed by drone-based photogrammetry. *Automation in Construction, 128*, 103787.

Vosselman, G., & Maas, H.-G. (2010). *Airborne and terrestrial laser scanning*: CRC press.

Voumard, J., Derron, M.-H., Jaboyedoff, M., Bornemann, P., & Malet, J.-P. (2018). Pros and Cons of Structure for Motion Embarked on a Vehicle to Survey Slopes along Transportation Lines Using 3D Georeferenced and Coloured Point Clouds. *Remote Sensing, 10*(11), 1732.

Ward, A. B., & Newman, J. K. (2019). *Assessment of LiDAR and Photogrammetry based Airfield Roughness Profiling Techniques*. ERDC Vicksburg United States.

White, R. A., Dietterick, B. C., Mastin, T., & Strohman, R. (2010). Forest roads mapped using LiDAR in steep forested terrain. *Remote Sensing, 2*(4), 1120-1141.

Zak, J. (2016, June). On laser scanning, pavement surface roughness and international roughness index in highway construction. In *Proceedings of the 6th Eurasphalt & Eurobitume Congress, Prague, Czech Republic* (pp. 1-3).

Zeybek, M., & Biçici, S. (2021). 3D Dense Reconstruction of Road Surface from UAV Images and Comparison of SfM Based Software Performance. *Turkish Journal of Remote Sensing and GIS, 2*(2), 96-105.

Appendix A

ArcGIS workflow with pane parameters:

Appendix B

Poster for 2022 Region 10 Transportation Conference:

School of Civil and Construction Engineering

ASSESSING THE ACCURACY AND FEASIBILITY OF UTILIZING UAS-BASED POINT CLOUD IN PAVEMENT SMOOTHNESS/ROUGHNESS MEASUREMENT

Fatih Sen, Erzhuo Che, Chase Simpson

Oregon State University

BACKGROUND

The driving quality and highway safety are critical quality indicators that transportation agencies are continuously striving to improve and are highly correlated with the smoothness of the road. To standardize the smoothness (or) roughness metrics, the International Roughness Index (IRI), calculated from longitudinal profile data collected on the road, was widely adopted. Structure of Motion (SfM) approach has lately been extensively utilized owing to their ability to reconstruct 3D information of structures and the associated textures. Especially, the uncrewed aircraft system (UAS) is highly efficient in gathering rich information in a local area. The core question regarding this method is whether the point clouds generated with such techniques can be utilized for measuring the pavement roughness (e.g., IRI) with sufficient accuracy. To answer this question, this study aims to establish a framework to attain IRI metrics from point cloud and assess its accuracy.

DATA COLLECTION

The project was carried out in southern Oregon coast along U.S. Highway 101 where there is an active landslide, named Arizona Inn. A control network was established with 10 ground control points (GCPs) set up along the shoulders surrounding the targeted road section. UAV-SfM data acquisition was performed with DJI-Phantom 4 RTK at 48.8m flight altitude. Additionally, 1062 image were collected with 1.36 cm/pix ground resolution. Additionally, a total of 17 terrestrial lidar scans with images were collected using Riegl VZ-400 to cover road section of interest, which served as reference in the following analysis.

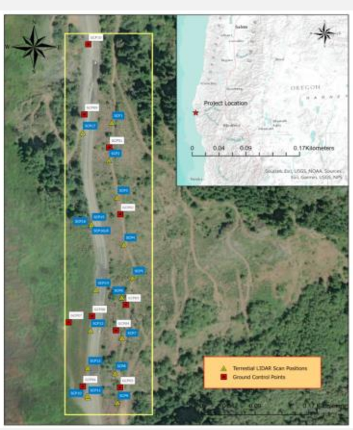

WORKFLOW

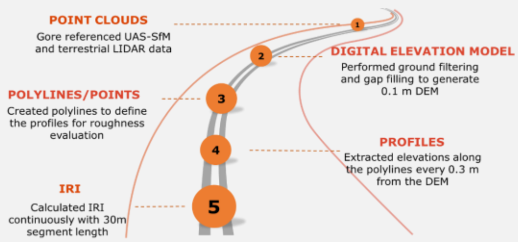

RESULT & ANALYSIS

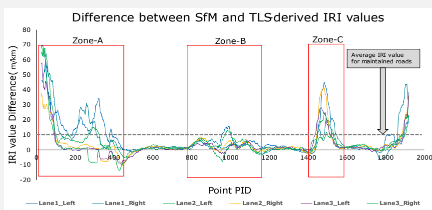

Statistical Summary of the IRI Value Comparison (m/km)						
	Lane 1 Left	Lane 1 Right	Lane 2 Left	Lane 2 Right	Lane 3 Left	Lane 3 Right
Minimum	-3.1	-6.5	-5.3	-10.8	-9.8	-13.8
Maximum	69.7	58.6	69.6	41.3	57.8	67.5
Median	2.8	1.9	2.4	1.7	1.2	1.0
Average	7.6	6.5	5.1	3.6	3.1	2.9
STD. Dev	11.4	11.5	9.1	8.3	8.6	10.2

ZONE-A

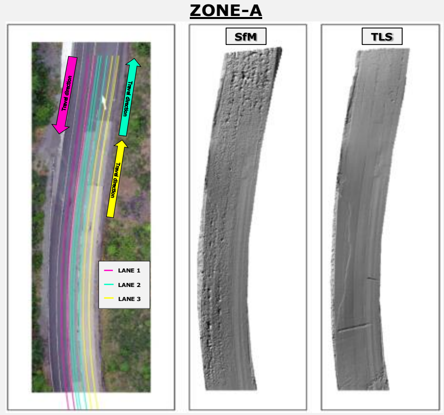

Note: Left/right definitions of the lanes are set with respect to travel direction

Statistical Summary of the IRI Value Comparison for Zone-A (m/km)						
	Lane 1 Left	Lane 1 Right	Lane 2 Left	Lane 2 Right	Lane 3 Left	Lane 3 Right
Minimum	3.7	0.8	-1.2	-8.3	-8.8	-13.8
Maximum	69.5	58.3	69.5	37.7	57.8	67.8
Median	16.3	11.1	7.6	2.4	0.6	0.8
Average	20.2	17.8	12.0	5.0	5.1	7.0
Std. Dev.	14.1	15.9	14.8	10.3	14.6	20.3

CHECK LANE

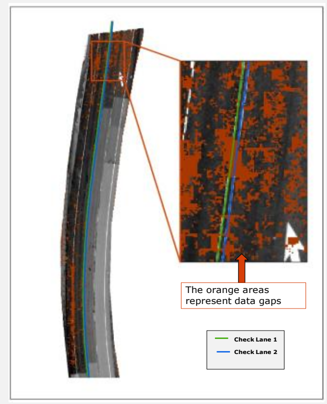

IRI Values Difference Statistics for Zone-A (m/km)		
	Check Lane 1	Check Lane 2
Minimum	0.0	-6.0
Maximum	99.5	38.8
Median	9.1	1.8
Average	22.4	4.3
Std. Dev.	26.8	9.7

CONCLUSION

Lesson learned

- Texture has a direct impact on SfM process and its derivative DEMs, which is why darker and texture-less surfaces have adverse effects on IRI computations.
- The IRI difference between SfM and TLS ranges from 2.9 to 7.6 (m/km) in this study. The standard deviations, another aspect of accuracy, are high due to the object texture, georefencing accuracy, ground filtering performance, and other factors,.
- To provide accurate estimates for smaller areas, the ProVAL requires a 20-meter buffer zone between the beginning and end of the project's AOI.

Future possibilities/ explorations

- The other zones(Zone B and Zone C) also needs to be investigated
- Re-investigate the check lane analysis with higher resolution SfM and TLS data

Oregon Department of Transportation
DAVID EVANS AND ASSOCIATES INC.
Leica Geosystems
MAPTEK

Appendix C

Poster for 3D Geo-Info 2021 Conference:

3D geoinfo

Assessing the Feasibility of Utilizing UAS-based Point Cloud in Pavement Smoothness/Roughness Measurement

Fatih Sen,[1] Erzhuo Che,[1] Chase Simpson[1]

1. School of Civil and Construction Engineering, Oregon State University

Oregon State University

BACKGROUND

The driving quality and highway safety are critical quality indicators that transportation agencies are continuously striving to improve and are highly correlated with the smoothness of the road. To standardize the smoothness/roughness metrics, the International Roughness Index (IRI), calculated from longitudinal profile data collected on the road, was widely adopted. Structure of Motion (SfM) approach has lately been extensively utilized owing to their ability to reconstruct 3D information of structures and the associated textures. Especially, the uncrewed aircraft system (UAS) is highly efficient in gathering rich information in a local area. The core question regarding this method is whether the point clouds generated with such techniques can be utilized for measuring the pavement roughness (e.g., IRI) with sufficient accuracy. To answer this question, this study aims to establish a framework to attain IRI metrics from point cloud and assess its accuracy.

WORKFLOW

- POINT CLOUDS — Georeferenced UAS-SfM and terrestrial lidar data
- DIGITAL ELEVATION MODEL — Performed ground filtering and gap filling to generate 0.1 m DEM
- POLYLINES/POINTS — Created polylines to define the profiles for roughness evaluation
- PROFILES — Extracted elevations along the polylines every 0.3 m from the DEM.
- IRI — Calculated IRI continuously with 30m segment length

DATA COLLECTION

The project was carried out in southern Oregon coast along U.S. Highway 101 where there is an active landslide, named Arizona Inn. A control network was established with 10 ground control points (GCPs) set up along the shoulders surrounding the targeted road section. UAV-SfM data acquisition was performed with DJI-Phantom 4 RTK at 48.8m flight altitude. Additionally, 1062 image were collected with 1.36cm/pix ground resolution. Additionally, a total of 17 terrestrial lidar scans with images were collected using Riegl VZ-400 to cover road section of interest, which served as reference in the following analysis.

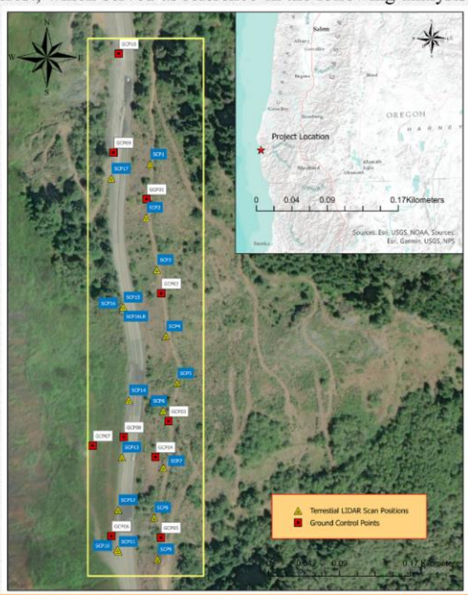

RESULTS & ANALYSIS

ELEVATION DIFFERENCECES						
(m)	Profile 1	Profile 2	Profile 3	Profile 4	Profile 5	Profile 6
MIN	-0.018	-0.074	-0.013	-0.044	-0.007	-0.011
MAX	0.084	0.075	0.086	0.151	0.103	0.083
MEDIAN	0.020	0.022	0.021	0.020	0.021	0.021
MEAN	0.020	0.020	0.020	0.020	0.020	0.021
STD.DEV	0.019	0.019	0.019	0.019	0.018	0.018

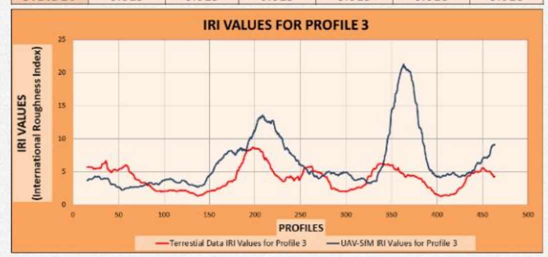

IRI VALUES DIFFERENCES						
(m/km)	Profile 1	Profile 2	Profile 3	Profile 4	Profile 5	Profile 6
MIN	-3.11	-1.38	-3.52	-7.91	-4.84	-6.70
MAX	9.84	28.19	16.65	19.75	10.70	6.86
MEDIAN	1.92	2.02	1.72	1.18	1.05	2.39
MEAN	2.77	3.44	2.44	1.83	1.22	1.77
STD.DEV	3.20	4.81	3.80	4.66	2.68	2.68

REFERENCES

[1] ASTM. (E1926 – 08 (Reapproved 2021)). *Standard Practice for Computing International Roughness Index of Roads from Longitudinal Profile Measurements* (Vol. 04.03). ASTM International.

PACTRANS · Leica Geosystems · Oregon Department of Transportation · NSF · David Evans and Associates Inc. · MAPTEK

Contact: senf@oregonstate.edu